AGU PUBLICATIONS

JGR

Journal of Geophysical Research: Space Physics

RESEARCH ARTICLE
10.1002/2015JA021642

Key Points:
- Postequinox, Saturn's PPOs abruptly change behavior every ~100–200 days
- Enhanced solar wind dynamic pressure and density associated with these changes
- PPO behavior possibly modulated by changes in the size of Saturn's magnetosphere

Supporting Information:
- Figures S1–S9
- Figures S1–S9 captions

Correspondence to:
G. Provan,
gp3@ion.le.ac.uk

Citation:
Provan, G., C. Tao, S. W. H. Cowley, M. K. Dougherty, and A. J. Coates (2015), Planetary period oscillations in Saturn's magnetosphere: Examining the relationship between abrupt changes in behavior and solar wind-induced magnetospheric compressions and expansions, *J. Geophys. Res. Space Physics*, *120*, 9524–9544, doi:10.1002/2015JA021642.

Received 2 JUL 2015
Accepted 11 OCT 2015
Accepted article online 14 OCT 2015
Published online 21 NOV 2015

Planetary period oscillations in Saturn's magnetosphere: Examining the relationship between abrupt changes in behavior and solar wind-induced magnetospheric compressions and expansions

G. Provan[1], C. Tao[2], S. W. H. Cowley[1], M. K. Dougherty[3], and A. J. Coates[4]

[1]Department of Physics and Astronomy, University of Leicester, Leicester, UK, [2]Research Institute in Astrophysics and Planetology, Université de Toulouse, UPS-OMP/CNRS, Toulouse, France, [3]Blackett Laboratory, Imperial College London, London, UK, [4]Mullard Space Science Laboratory, University College London, Dorking, UK

Abstract We examine planetary period oscillations (PPOs) observed in Saturn's magnetospheric magnetic field data from the time of Saturn's equinox in 2009. In particular, we focus on the time period commencing February 2011, when the oscillations started to display sudden and unexpected changes in behavior at ~100–200 day intervals. These were characterized by large simultaneous changes in the amplitude of the northern and southern PPO systems, together with small changes in period and jumps in phase. Nine significant abrupt changes have been observed in the postequinox interval to date, commencing as the Sun started to emerge from a long extended solar minimum. We perform a statistical study to determine whether these modulations in PPO behavior were associated with changes in the solar and/or upstream solar wind conditions. We report that the upstream solar wind conditions show elevated values of solar wind dynamic pressure and density around the time of PPO behavioral transitions, as opposed to before and after these times. We suggest that abrupt changes in PPO behavior may be related to significant changes in the size of the Saturnian magnetosphere in response to varying solar wind conditions.

1. Introduction

Saturn is the only planet within our solar system that has, at least by all measurements to date, a near-perfectly axisymmetric magnetic field [e.g., *Burton et al.*, 2010]. Despite this, however, oscillations with a period near the ~11 h planetary period are observed throughout Saturn's magnetosphere. Such modulations are observed in the magnetic field, Saturnian kilometric radiation (SKR), plasma parameters, energetic particle fluxes, and associated neutral atom emissions, as well as auroral ultraviolet, infrared, and radio emissions [e.g., *Warwick et al.*, 1981, 1982; *Desch and Kaiser*, 1981; *Gurnett et al.*, 1981, 2007, 2010a; *Sandel and Broadfoot*, 1981; *Sandel et al.*, 1982; *Carbary and Krimigis*, 1982; *Espinosa and Dougherty*, 2000; *Krupp et al.*, 2005; *Cowley et al.*, 2006; *Kurth et al.*, 2007; *Southwood and Kivelson*, 2007; *Carbary et al.*, 2007, 2008a, 2008b; *Zarka et al.*, 2007; *Andrews et al.*, 2008; *Nichols et al.*, 2008, 2010a, 2010b; *Burch et al.*, 2009; *Provan et al.*, 2009a, 2009b; *Clarke et al.*, 2006; *Badman et al.*, 2012; *Lamy et al.*, 2013]. Those oscillations were first observed in Voyager measurements of the SKR emissions, around the time of Saturn's northern hemisphere spring equinox [*Kaiser et al.*, 1980]. *Desch and Kaiser* [1981] reported a dominant oscillation with a period of 10 h 39 m 24 ± 7 s (10.6567 ± 0.0019 h) (subsequently modified to 10.6562 h in *Davies et al.* [1983]) which was used to define the International Astronomical Union System III rotation period. Radio polarization measurements indicate that this oscillation was observed in emissions from Saturn's northern hemisphere. *Desch and Kaiser* [1981] also reported a second oscillation, considerably weaker but still statistically significant, with a period of 10.69 h. *Provan et al.* [2014] tentatively attributed this second period to emissions from the southern hemisphere.

Cassini observations of SKR emissions and magnetic field oscillations have demonstrated that there are indeed two planetary period oscillation (PPO) systems present, one related to each hemisphere, which rotate about the planetary axis with slightly different periods [*Kurth et al.*, 2008; *Gurnett et al.*, 2009a, 2009b; *Andrews et al.*, 2010b]. The PPO periods determined from the SKR and magnetic field data sets are, in general, in very close agreement, as reported by *Andrews et al.* [2010b, 2012] and *Provan et al.* [2014]. SKR observations made by the Ulysses spacecraft in 1997 detected periods that were not constant and varied by 1% from the Voyager values [*Galopeau and Lecacheux*, 2000]. *Cecconi and Zarka* [2005] attempted to explain the slow variability, and possible

multiplicity, of Saturn's radio period by modeling the role of the Kelvin-Helmholtz instability on the SKR source and the influence of the observed sawtooth variations in solar wind speed on the local time position of the source. *Cecconi and Zarka* [2005] also studied the role of noise in the SKR phase modulation by the solar wind speed. The existence of these small variations was confirmed by radio measurements from the Cassini spacecraft [*Gurnett et al*., 2005]. *Gurnett et al*. [2009a, 2010b] suggested that such variations might be driven by seasonal variations in solar UV flux resulting in the modulation of ionospheric conductivity. Higher conductivity in the sunlit summer hemisphere would increase the strength of the field-aligned currents thereby increasing the coupling of the polar hemisphere with the plasma disk. This would result in slower PPO periods in the summer hemisphere compared with the winter hemisphere. According to *Gurnett et al*. [2009a], this solar illumination picture would require a reversal of the SKR rotation rates in the two hemispheres at Saturn's equinox.

In section 3, we will present a summary of the PPO periods from the time of Voyager until the time of writing (early 2015), presenting data from Voyager, Ulysses, and Cassini. It is clear from these results that the periods of the PPOs have not crossed as predicted by the solar illumination picture, as previously reported by *Andrews et al*. [2012]. However, a number of abrupt changes in the phases, periods, and amplitudes of the two oscillations have been observed with a cadence of 100–200 days, as reported by *Provan et al*. [2013]. Further, *Provan et al*. [2011] reported unexplained behavior of the PPO oscillations observed within Saturn's near-equatorial core ($L < 12\ R_s$) magnetosphere between 2004 and 2006, observing short-term (pass-to-pass) variation of the magnetic phase common to all field components, consistent with pass-to-pass variations in the PPO periods. Similar observations have previously been reported by *Zarka et al*. [2007], who reported fluctuations in the SKR period with a characteristic timescale of 20–30 days associated with variations in the solar wind velocity. When considering which factors may be influencing the behavior of the PPO periods, it is worth noting that it is not just Saturn's seasons that have changed during the 11 year long Cassini mission but that solar activity has also been strongly varying. A Saturnian season (e.g., a northern or southern spring/summer) lasts for ~15 years, while a solar cycle has an approximate duration of 11 years, so the seasonal and solar effects are changing on similar timescales. The initial Cassini mission, from 2004 to 2007, occurred in the late declining phase of the solar cycle. The mission then continued during the extended solar minimum occurring from 2007 to 2010. An increase in solar activity was observed to commence in 2011.

Previous results have demonstrated changes in the behavior of the SKR associated with the solar wind. *Desch* [1982] analyzed data from Voyager 1 and 2 to establish that Saturn's radio emissions underwent extreme fluctuations in the radio energy on a timescale of days to weeks. Correlation coefficients of ~0.6 were determined at lag times of 0–1 days between the arrival at Saturn of high-speed solar wind streams and the onset of increased radio emissions. *Desch and Rucker* [1983] reported that fluctuations in SKR power were best correlated with solar wind ram pressure variations. Using a 170 day analysis interval, they also reported a close correlation with solar wind density and fluctuations in SKR emissions and a weaker correlation with solar wind speed. It is worth noting that such fluctuation in SKR emissions will be associated with the occurrence of Saturn "auroral storms." These storms have been reported by *Meredith et al*. [2014] to have a typical cadence of ~5 days, thus occurring more frequently than the changes in behavior of the PPOs.

As mentioned above, *Zarka et al*. [2007] reported fluctuations in the SKR period with a characteristic timescale of 20–30 days associated with variations in the solar wind velocity. *Badman et al*. [2008] demonstrated how emitted SKR power increased when the solar wind was compressed and also presented two case studies demonstrating reduction in emitted SKR power during times of reverse solar wind shocks. They also reported that the pulsing of the SKR during these disturbed intervals was not significantly altered relative to that during nondisturbed intervals.

Kimura et al. [2013] presented a long-term correlation analysis between SKR, solar EUV flux, and propagated solar wind parameters, where they focused on variations with timescales in excess of several weeks. The study was performed during southern hemisphere summer from 2004 to 2010 during the declining phase of the solar cycle. They reported positive correlations between solar wind dynamic pressure and peak EUV flux density in both hemispheres. They concluded that the northern and southern SKR were "in phase" with each other in terms of the solar wind response, suggesting possible simultaneous responses of northern and southern SKR sources to global solar wind compression. In contrast, they reported an "antiphase" relationship between the southern and northern SKR and the solar EUV flux, attributing this to seasonal variations in the solar illumination of each hemisphere.

Here we examine the origin of the ~100–200 day PPO variations discovered by *Provan et al*. [2013] and, in view of previous discussion of solar wind dependency of SKR modulations, will examine whether these could also

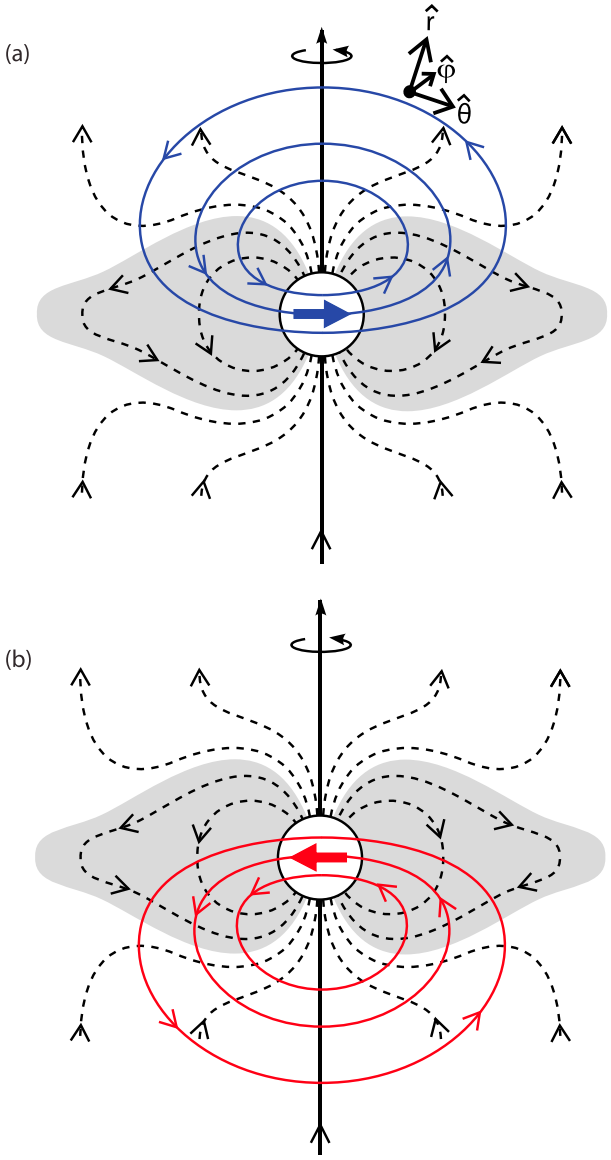

Figure 1. Sketch showing the spatial structure of (a) N and (b) S magnetic field oscillations as blue (Figure 1a) and red (Figure 1b) lines. The oscillations are shown in the principal meridian of the perturbation at some instant, where the vertical axis represents the spin (and magnetic) axis of the planet. The black dashed lines show the quasi-static "background" magnetospheric field, with closed field lines at lower latitudes (gray region) and open field lines at high latitudes (clear region) mapping into the N (S) polar regions. This perturbation field pattern then rotates approximately rigidly about the axis at the N (S) PPO period, giving rise to magnetic field oscillations at that period at a fixed point. In the equatorial region the perturbation field takes the form of a rotating quasi-uniform field with additional north-south components such that the field lines form arches with apices pointing to the north (south). In the northern (southern) high-latitude region the perturbation instead has the form of a planet-centered rotating transverse dipole, whose instantaneous direction is indicated by the large blue (red) arrow, having the same direction as the equatorial quasi-uniform field [from *Andrews et al.*, 2010b; *Provan et al.*, 2011].

have a solar wind or solar origin, noting that the onset of the PPO variations occurred in concert with an increase in solar activity. First, we will present a brief overview of the characteristics of the PPOs observed in the magnetic field data at Saturn.

2. Overview of the Form and Theoretical Analysis of Magnetic Field Oscillations

Below we summarize the form of the PPO magnetic systems previously reported in other publications [see, e.g., *Andrews et al.*, 2008, 2010a, 2010b, 2012; *Provan et al.*, 2011, 2013]. There are two magnetic perturbation systems which take the form of perturbation field loops, one closing over the northern (N) pole and the other over the southern (S) pole. The forms of the perturbation field loops are sketched in Figure 1. The blue loops in Figure 1a and the red loops in Figure 1b indicate the perturbation fields of the N and S systems, respectively, in their principal magnetospheric meridian planes at some instant of time. The black dashed lines indicate the near-axisymmetric unperturbed magnetospheric field, with closed lines in the equatorial region (gray) and open lines extending into the tail at high latitudes (clear). Both loops pass through the equatorial "core" magnetosphere ($L < 12\,R_s$), where they form quasi-uniform magnetic fields. The N (S) field perturbation then closes over the N (S) polar region, forming quasi-dipolar magnetic fields. The perturbation fields out of these planes can be pictured to a first approximation simply by displacing the loops directly into and out of the plane of the figure. These two field patterns then rotate independently about the planetary spin axis at the periods of the southern and the northern systems, respectively.

It is possible to distinguish between N and S oscillations, and between core (quasi-uniform) and polar (quasi-dipolar) oscillations, based on their polarization characteristics. As can be seen in Figure 1, for purely S oscillations the radial (r) and colatitudinal (θ) components are in phase, while for purely N oscillations the r and θ components are in antiphase with each other. This applies to both the equatorial quasi-uniform and the polar quasi-dipolar oscillations. However,

Table 1. Polarization Characteristics of Northern and Southern PPOs

Southern Core Oscillations

	Core r $\gamma_{rs}\equiv 0°$	Core θ $\gamma_{\theta s}=0°$	Core φ $\gamma_{\varphi s}=90°$
Core r $\gamma_{rs}\equiv 0°$	-	θ and r in-phase	φ in lagging quadrature with r
Core θ $\gamma_{\theta s}=0°$	r and θ in-phase	-	φ in lagging quadrature with θ
Core φ $\gamma_{\varphi s}=90°$	r in leading quadrature with φ	θ in leading quadrature with φ	-

Northern Core Oscillations

	Core r $\gamma_{rN}\equiv 0°$	Core θ $\gamma_{\theta N}=180°$	Core φ $\gamma_{\varphi N}=90°$
Core r $\gamma_{rN}\equiv 0°$	-	θ and r in anti-phase	φ in lagging quadrature with r
Core θ $\gamma_{\theta N}=180°$	r and θ in anti- phase	-	φ in leading quadrature with θ
Core φ $\gamma_{\varphi N}=90°$	r in leading quadrature with φ	θ in lagging quadrature with φ	-

Southern Polar Oscillations

	Polar r $\gamma_{rs}\equiv 0°$	Polar θ $\gamma_{\theta s}=0°$	Polar φ $\gamma_{\varphi s}=-90°$
Polar r $\gamma_{rs}\equiv 0°$	-	θ and r in-phase	φ in leading quadrature with r
Polar θ $\gamma_{\theta s}=0°$	r and θ in-phase	-	φ in leading quadrature with θ
Polar φ $\gamma_{\varphi s}=-90°$	r in lagging quadrature with φ	θ in lagging quadrature with φ	-

Northern Polar Oscillations

	Polar r $\gamma_{rN}\equiv 0°$	Polar θ $\gamma_{\theta N}=180°$	Polar φ $\gamma_{\varphi N}=-90°$
Polar r $\gamma_{rN}\equiv 0°$	-	θ and r in anti-phase	φ in leading quadrature with r
Polar θ $\gamma_{\theta N}=180°$	r and θ in anti- phase	-	φ in lagging quadrature with θ
Polar φ $\gamma_{\varphi N}=-90°$	r in lagging quadrature with φ	θ in leading quadrature with φ	-

for quasi-uniform oscillations for either system the φ component is in lagging quadrature with r, while for the quasi-dipolar oscillations for either system the φ component is in leading quadrature with r, thus leading directly to the quasi-uniform and quasi-dipolar form of these fields. The polarization characteristics of the purely northern and purely southern PPOs are described in Table 1, which also presents, $\gamma_{i\,S,N}$, the difference in phase between the r component and component i, where $i = r$, θ, and φ, such that by definition $\gamma_{r\,S}\equiv 0°$ and $\gamma_{r\,N}\equiv 0°$. For further explanation of the polarization of the northern and southern oscillations, see *Provan et al.* [2009a].

The N and S PPO-related magnetic field perturbations can then be expressed, for spherical polar field component $i = (r,\ \theta,\ \varphi)$, referenced to the planetary spin and magnetic axes, as an "$m = 1$" rotating field of the following form:

$$B_i = B_{0S,Ni}\cos\left(\Phi_g(t) - \varphi - \psi_{iS,N}(t)\right) = B_{0S,Ni}\cos\left(\Phi_{S,N}(t) - \varphi\right). \quad (1)$$

In these expressions Φ_g is the phase of the guide oscillation whose period, of 10.68 h, has been selected to be close to the period of the oscillations, $\psi_{iS,N}(t)$ is the phase of the oscillations with respect to the N or S guide phase, $\Phi_{N,S}(t) = \Phi_g(t) - \psi_{iS,N}$ are the phases of the N or the S PPO perturbations, $B_{0S,N\,i}$ are the amplitudes of the N or S oscillations, and φ is azimuth measured from local noon.

The corresponding periods are given by

$$\tau_{N,S} = \frac{360}{\left(\frac{d\Phi_{N,S}}{dt}\right)}, \tag{2}$$

where the phases are expressed in degrees.

Andrews et al. [2008] have described how ψ_i is determined for each of the three components of the magnetic field on an orbit-by-orbit basis by a cross-correlation analysis between the observed oscillations and an oscillation at a guide period selected to be close to the period of the oscillations. The ψ_i phases are then plotted versus time, relative to a suitable guide phase, in the S and N format. This involves subtracting the difference in the polarization angle between the r and θ components and the r and the φ components (as described by $\gamma_{i\,S,N}$ presented in Table 1) from the θ and the φ components (see Figures 3d and 3e introduced below). If only the northern or the southern oscillations are present, the three components of the southern or northern formatted phases should then all have the same values (within errors), equal to the phase of the r component. *Andrews et al.* [2012] reported that within the northern or southern polar region only the pure northern or southern oscillations are observed, within 10% amplitude measurement uncertainty. However, *Provan et al.* [2011] reported that within the core region organized "jitter" of the phases occurs due to both oscillations being simultaneously present, where they constructively and destructively interfere at the beat period of the two oscillations, leading to more complex phase and amplitude relationships of the combined oscillations [*Andrews et al.*, 2012; *Provan et al.*, 2013]. The superposition of the two oscillations within the core regions can be described by

$$B_i(\varphi, t) = B_{0i}(t)\cos(\Phi_i(t) - \varphi) = B_{0Ni}\cos(\Phi_N(t) - \varphi - \gamma_{i\,N}) + B_{0Si}\cos(\Phi_S(t) - \varphi - \gamma_{i\,S}) \tag{3}$$

This superposition is then dependent on the beat phase of the two oscillations and the relative amplitude of the two oscillations. The amplitude ratio of the northern to southern oscillations for component i is

$$k = B_{0Ni}/B_{0Si}, \tag{4}$$

where this ratio is assumed to be the same for each field component. If $k < 1$, then the southern oscillations are dominant within the core region, while if $k > 1$, the northern oscillations are dominant. If $k = 1$, the two oscillations have equal amplitude within the core. The beat phase of the oscillations is defined by

$$\Delta\Phi_B(t) = \Phi_N(t) - \Phi_S(t), \tag{5}$$

the beat period being given by $\tau_B(t) = 360/(d\Delta\Phi_B/dt)$ for $\Delta\Phi_B(t)$ expressed in degrees.

The superposition of these two oscillation results in phase jitter between the r and θ components and between the φ and θ components, as described by *Andrews et al.* [2012] for the southern oscillation by

$$\Delta\psi_{r-\theta}(t) = \Delta\psi_{\varphi-\theta}(t) - \gamma_{\varphi S} = -\tan^{-1}\left[\frac{2k\sin\Delta\Phi_B}{1-k^2}\right]. \tag{6}$$

Andrews et al. [2012] showed how the N and S phases, $\Phi_{N,S}(t)$, periods $\tau_{N,S}(t)$, and amplitude ratios k can then be calculated by piecewise linear fits to the S and N format data employing successive sets of 25 data points typically spanning ~200 days. Each fit is taken to define the phase and period of the S and N system oscillations at the center time of the data set employed. The sequence of such values obtained from data sets shifted one data point at a time, typically separated by ~10 days, with linear interpolation between, is then taken to define these quantities over time. While this procedure was successfully applied by *Andrews et al.* [2012] to Cassini data observed up to early 2011, it was deemed inappropriate to apply this technique to data observed after this time due to the abrupt changes in the PPO behavior. For data observed between 2011 and mid-2013, *Provan et al.* [2013] simply employed piecewise linear fits to the individual intervals containing near-steady oscillation properties. Here this analysis has been extended through to the end of 2014 as detailed in section 4. It is worth noting that *Provan et al.* [2013] demonstrated that five-parameter fits (two linear phases and k) to 150 day segments of phase data evaluated every 50 days show essentially similar results to the results provide by *Andrews et al.* [2012].

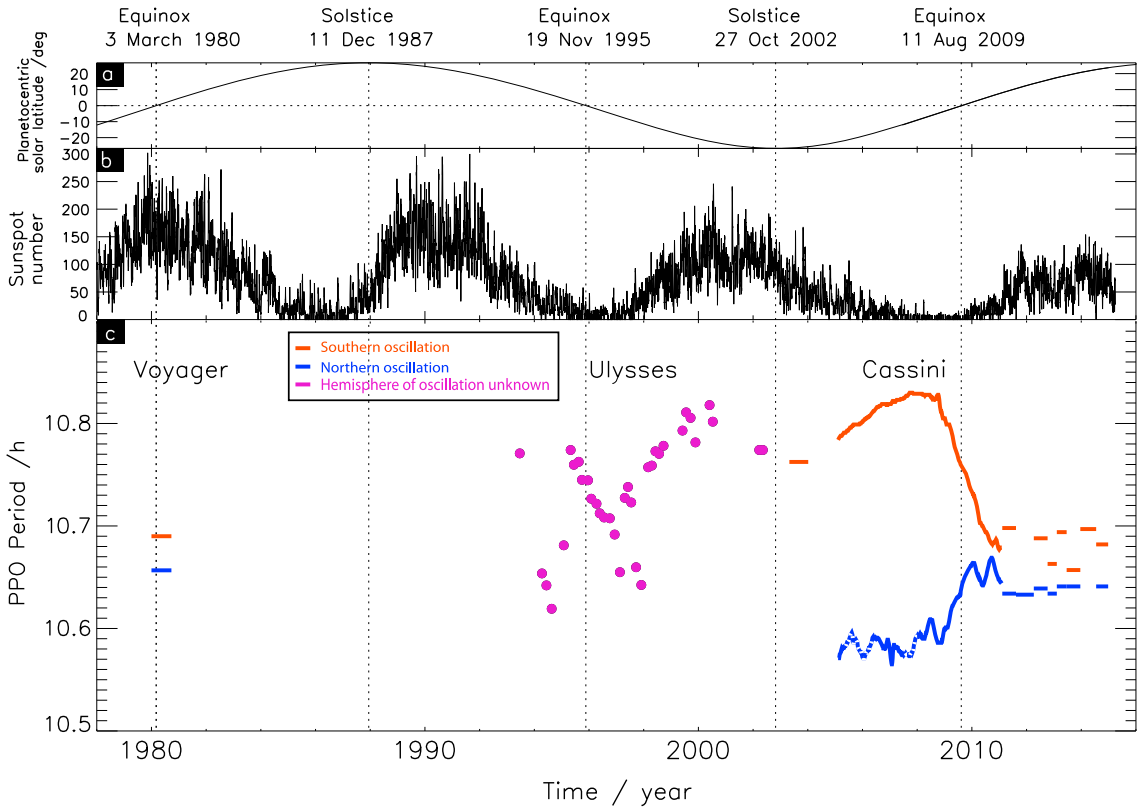

Figure 2. Plots showing (a) the planetocentric latitude of the Sun at Saturn (deg), (b) the daily sunspot number, and (c) the PPO rotation periods (in hours) derived from Voyager, Ulysses, and Cassini measurements as indicated. The vertical dotted lines indicate Saturn's seasons, specifically the northern and southern summer solstices where the solar latitude is maximum and minimum, respectively, and the equinoxes where the latitude passes through zero. The northern and southern PPO periods determined from the Voyager and Cassini data are shown by the blue and red lines, respectively, while the Ulysses data are shown by purple dots since the corresponding hemisphere remains undetermined from direct measurement of their polarization.

3. Summary of Previous Observations

Figure 2 presents a summary of observational knowledge of the S and N PPO periods from the time of Voyager until the end of 2014. Figure 2a presents the planetocentric latitude of the Sun at Saturn, exhibiting the changing seasons. The figure encompasses slightly more than one Saturn year, from vernal equinox (March 1980) during the Voyager era to autumnal equinox (November 1995) spanned by the Ulysses data and southern summer and vernal equinox (August 2009) again during the Cassini era. Figure 2b presents the daily number of sunspots from the OMNI website (http://omniweb.gsfc.nasa.gov) clearly exhibiting variations with the solar cycle. Both solar activity and solar illumination change over time. The Voyager spacecraft arrived at Saturn when the Sun was at solar maximum during Saturn's northern hemisphere spring equinox in 1980. Both the Ulysses and the Cassini observations commence during the declining phase of one solar cycle and continue through the rising phase and maximum of the following solar cycle. However, Ulysses' first observations were made during northern hemisphere summer, while Cassini's initial observations were made during southern hemisphere summer. Much of the detailed analysis in this paper will focus on the observations made during the northern spring equinox of 2009 when the solar cycle was in an extended minimum and after this time when solar activity started to increase again.

Figure 2c presents the PPO periods (hours), where we have combined the results of analyses of SKR data from the Voyager approach interval in 1980 [*Desch and Kaiser*, 1981], Ulysses remote sensing during 1993–2002 [*Galopeau and Lecacheux*, 2000; *Gurnett et al*., 2010b], and Cassini observations from planetary approach in 2003–2004 (horizontal red bar) [*Gurnett et al*., 2005]. The periods from Cassini approach and in situ observations from 2004 to 2014 have been determined from magnetic field observations as has previously described above, although here the analysis has been extended to the end of 2014 to include the most recent data.

The southern period is shown in red and the northern period in blue. The Ulysses data are shown in purple, since its hemisphere of origin is not known.

The periods show a strong seasonal dependence. When PPOs were first observed in the Voyager data, over one Saturnian year ago, the two periods were fairly close with a northern period of ~10.65 h and a southern period of 10.69 h. When Ulysses first started observing SKR in 1993, almost half a Saturnian year later, the spacecraft observed two well-separated periods. The two periods then started to converge a year prior to autumnal equinox and appear to meet approximately a year after the 1995 southern vernal equinox. As the hemisphere of origin of the oscillations is not known, it is not possible to identify whether the two periods crossed or whether they simply converged and then diverged again, but it is clear that when Cassini arrived at Saturn in 2004 during southern hemisphere summer, the two periods were well separated with a northern period of ~10.55 h and a southern period of ~10.75 h. The two periods continued to diverge, with the southern period commencing a sharp decrease approximately a year prior to the 2009 southern autumnal equinox. The two periods come to their closest value approximately a year after equinox. After this, it was generally anticipated that the two periods would cross, but this did not happen. Instead, since 2011, the two periods have remained fairly stable. The southern period has remained consistently longer than the northern period, with the southern period being ~10.69 h and the northern period ~10.63 h. These periods are very similar to the Voyager observations made during Saturn's last postvernal equinox period. However, since 2011, there has been a new and unusual behavior of the oscillations, with the two oscillations presenting large jumps in amplitude, with associated small jumps in period and phase that will be discussed below. This unusual behavior commenced around the time that solar activity started to increase after a long extended minimum, as evidenced by an increase in the number of sunspots.

4. Magnetic Field Oscillations in the Postequinox Interval

Figure 3 presents the periods, amplitude ratio, and phases of the oscillations observed from the equinox in August 2009 up to and including Rev 212, which ended in February 2015. This plot thus covers data from $t = 2049$ to $t = 4077$ days (where $t = 0$ is 00:00 UT on 1 January 2004). Start of year markers are shown at the top of the plot (red) together with Cassini Rev markers (black) plotted at each periapsis and numbered every 10 Revs. The top bar identifies orbit-type based on Cassini's trajectory, with near-equatorial orbits shown in blue and highly inclined orbits shown in green. Following *Andrews et al.* [2012] and *Provan et al.* [2013, 2014], the equatorial orbits commencing just prior to equinox are labeled E1 to E4, and the series of polar orbits starting at Rev 176 are labeled F1 and F2. The second bar presents the new interval identifiers 1–9, demarked by vertical dashed lines also labeled from 1 to 9 identifying the times of nine PPO boundaries (see below). Figure 3a then shows the latitude of spacecraft periapsis (degrees) for each Rev (black dots), plotted at the time of periapsis, together with the latitude range of each Rev (vertical bars). Figure 3b presents the PPO periods (in hours) determined from the magnetic field oscillations; the N (S) period is shown in blue (red). Figure 3c presents the N/S amplitude ratio "k" of the oscillations within the core region of Saturn's magnetosphere (equation (4)). In the lower half of this panel the scale is linear in k from zero to unity, while in the top half of the panel the scale is linear in $1/k$ from unity to zero (i.e., k from unity to infinity). It is only possible to determine k for equatorial orbits where both oscillations are observed and for inclined orbits that also pass through the core magnetosphere.

Figures 3d and 3e present the phases of the oscillation in the S format ($\psi_i - \gamma_{iS}$) (N format ($\psi_i - \gamma_{iN}$)), determined on a Rev-by-Rev basis as described in section 2. For the radial (r), colatitudinal (θ), and azimuthal phase (φ) components, the phases are shown in red, green, and blue, respectively. Phases observed within the core magnetosphere are shown as filled circles, and phases observed within the S or N polar region are shown as open circles. The phases are plotted with respect to a guide phase with a similar period as the oscillations, the chosen S (N) guide period is 10.69 h (10.64 h).

Figure 3 demonstrates that in the postequinox interval there exist a number of abrupt transitions in the amplitude of the oscillations together with apparent smaller jumps in period and phase [*Provan et al.*, 2013]. These have a cadence of ~100–200 days, with nine transitions having been observed between the beginning of 2011 and the end of 2014. They are identified as occurring between one periapsis Rev and the next, except for boundary 8 where suitable N data were not available for Rev 206 and the boundary was then identified as occurring between Rev 205 and Rev 207. In the postequinox interval the periapsis of two Revs are typically separated by ~17–30 days, and we define the transition times to occur at the midtime between the times of two such periapsis. In previous papers [e.g., *Andrews et al.*, 2012; *Provan et al.*, 2013], these intervals have

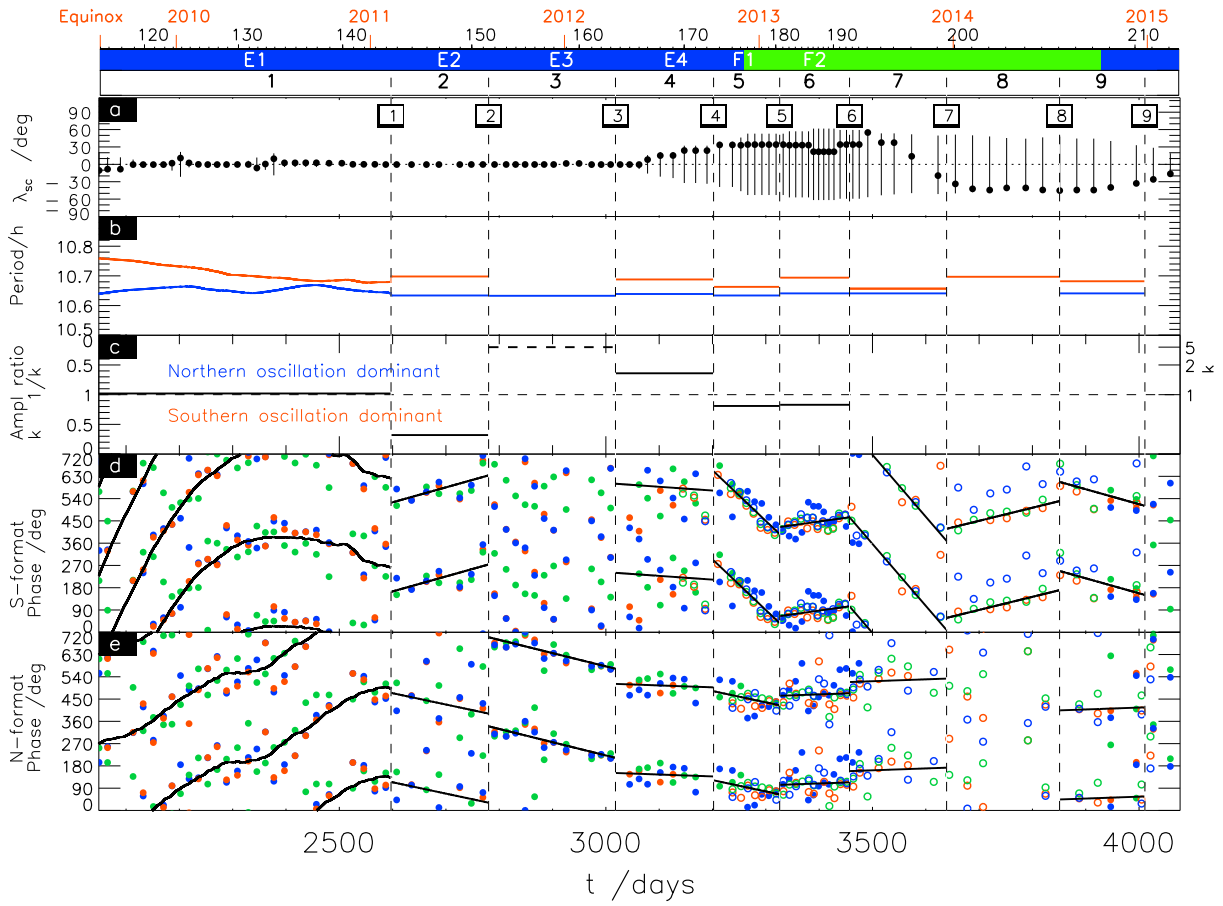

Figure 3. Plot showing PPO characteristics derived from magnetic field data throughout the Cassini mission versus time in days, from the equinox at 11 August 2009 ($t = 2049$) to 1 March 2015 ($t = 4077$) (with periods shown to the end of 2014, $t = 4017$). Start-of-year and Cassini Rev markers are shown at the top of the plot. The top bar shows the interval identifiers based on Cassini's trajectory consisting of near-equatorial orbits (blue bars) and highly inclined orbits (green bars), with the intervals labeled from E to F. The second bar presents interval identifiers defined by the rapid transition in PPO behavior. The intervals are labeled 1–9, demarked by vertical dashed lines also labeled from 1 to 9 marking the times of nine PPO boundaries. (a) Latitude of spacecraft periapsis (degrees) for each Rev (black dots), plotted at the time of periapsis, together with the latitude range of each Rev (vertical bars). (b) Rotation periods for the southern (red line) and northern (blue) PPOs. (c) The north/south magnetic oscillation amplitude ratio k (equation (4)), where in the lower half of the panel the scale is linear in k from zero to unity, while in the upper half it is linear in $1/k$ between unity and zero (corresponding to k values between unity and infinity as indicated on the right side of the panel). (d) Magnetic oscillation phase data ($\psi_i - \gamma_{iS}$) plotted in southern format relative to a core region guide phase corresponding to a fixed period of 10.69 h where red, green, and blue data correspond to the r, θ, and φ field components, respectively, while solid circles indicate phases derived from core region data and open circles indicate phases derived from southern polar magnetic field data. (e) Magnetic oscillation phase data ($\psi_i - \gamma_{iN}$) plotted in northern format, relative to a core region guide phase corresponding to a fixed period of 10.64 h, where solid circles indicate phases derived from the same core region phase data as in Figure 3d and open circles indicate phases derived from northern polar magnetic field data. Two full cycles of phase are plotted in the vertical axis of Figures 3d and 3e, with each data point being plotted twice. The black lines in Figures 3d and 3e show the southern and northern PPO phases, respectively, based on fits to these data.

been labeled based both on Cassini's trajectory combined with sequentially increasing numbers identifying the PPO boundaries. For example, the start of F2 occurred at the second PPO transition observed when Cassini is engaged in a series of polar orbits. However, with an ever increasing number of boundaries, this system has become rather unwieldy and here we have therefore introduced a new simplified nomenclature which is independent of Cassini's trajectory. The first PPO transition time demarked the start of interval E2 in the old nomenclature. Before this time the periods and the phases were believed to change slowly over time as presented in *Andrews et al.* [2008] and *Provan et al.* [2009a]. We here define this first PPO transition as boundary 1, with interval 1 spanning the time period just prior to the 2009 equinox until boundary 1. For simplicity the next interval is now called interval 2 with the interval ending at boundary 2. The next seven boundaries and intervals are all labeled sequentially, and all nine intervals are identified in the second bar at the top of Figure 3. The boundaries are labeled with numbers within black boxes, and all boundary times are presented in Table 2.

Table 2. Times of the PPO Boundaries (Where $t = 0$ Is 00:00 UT on 1 January 2004)

Boundary	Rev Before Boundary	Rev After Boundary	Time of Periapsis Before Boundary (t)	Time of Periapsis After Boundary (t)	Boundary Time (t)	Boundary Time (Year, Month, Day)
1	144	145	2587.12	2607.57	2597.35	2011, 2, 10
2	151	152	2769.34	2791.17	2780.25	2011, 8, 12
3	163	164	3008.90	3026.71	3017.80	2012, 4, 5
4	172	173	3189.62	3213.38	3202.50	2012, 10, 7
5	180	181	3319.23	3332.53	3325.88	2013, 2, 7
6	192	193	3451.25	3463.21	3457.23	2013, 6, 19
7	199	200	3622.97	3655.48	3639.21	2013, 12, 18
8	205	207	3819.30	3883.241	3851.27	2014, 7, 18
9	210	211	3994.88	4026.75	4010.82	2014, 12, 24

At the time of Saturn's equinox in August 2009, the N and S oscillations had approximately equal amplitudes within Saturn's core magnetospheric region with $k \sim 1$. Boundary 1 occurred in mid-February 2011 ($t = 2597$ days). It was characterized by a sharp resumption of southern amplitude dominance, with $k \sim 0.32$, which was unexpected during the northern spring condition. Boundary 2 occurred toward the middle of 2011 and introduced strong northern dominance for the first time in this data set with $k \geq 5$. During this time no S oscillations were detectable in the equatorial magnetic data, such that no S phase or southern period is shown in the figure. The lack of detectability of a separate southern oscillation in equatorial data is indicative that its amplitude is more than 5 times less than that of the observed northern oscillations as reported by *Provan et al.* [2013]. Boundary 3 occurred at the start of Rev 164 in 2012, where for the first time in these data, the core region amplitudes in all three field components were sufficiently low (~0.2–0.4 nT) that no phases could reliably be determined. Over the following Revs, the amplitudes then recovered to more normal values such that phases can once more be determined. During interval 4 the amplitude of the southern oscillations increased and the amplitude of the northern oscillations decreased with respect to interval 3. However, the northern oscillations were still dominant in the equatorial plane with $k \sim 1.5$. Unexpectedly, weak south dominance resumed in late 2012 and continued to at least mid-2013 with $k \sim 0.8$ for intervals 5 and 6. Due to the inclined nature of the trajectories after this time, equatorial observations were no longer possible and so amplitude ratios could not be determined.

During interval 8 the southern polar oscillations demonstrated unusual polarization behavior. As outlined in section 2, in the southern polar region we expect to observe a quasi-dipolar field with the azimuthal field component in leading quadrature with the radial and colatitudinal components. However, during interval 8, although the radial and colatitudinal phase components remained in phase, the azimuthal phase values were approximately in phase with the radial and colatitudinal phases. This is an unexpected discovery and will be explored in a subsequent paper. The period of the southern oscillations for interval 8 was therefore only determined from the r and θ component values. Further, it has not been possible to determine a northern period for interval 8 due to the scattered northern phase values. We believe that this is due to the nature of Cassini's trajectory on these Revs, with periapsis close to the planet in the southern hemisphere while apoapsis is in the northern hemisphere and predicted to be located beyond Saturn's bow shock on many Revs. The observed oscillations would then include a significant radial phase delay, with signatures of magnetopause and bow shock crossings also present within the magnetic field data. By interval 9, which ended in December 2014, the northern period was ~10.64 h and the southern period was ~10.68 h. Thus, overall the two PPO periods remained fairly stable over intervals 1 to 9, albeit with abrupt changes in southern period associated with abrupt changes in the relative amplitudes.

5. Solar and Solar Wind Data

In Figure 4 we present solar and solar wind data from the 2009 equinox ($t = 2049$ days) until 1 March 2015 ($t = 4077$ days). Figure 4a again presents the PPO period as in Figure 3b, with the times of the nine boundaries marked with dashed black lines. Figures 4b–4e present propagated solar wind data determined using a one-dimensional MHD propagation of the solar wind measurements from 1 AU to Saturn using observations from the two STEREO spacecraft and OMNI near-Earth solar wind data. The propagation method is described in *Tao et al.* [2005]. In this plot, and throughout the paper, we have amalgamated the three propagated solar wind

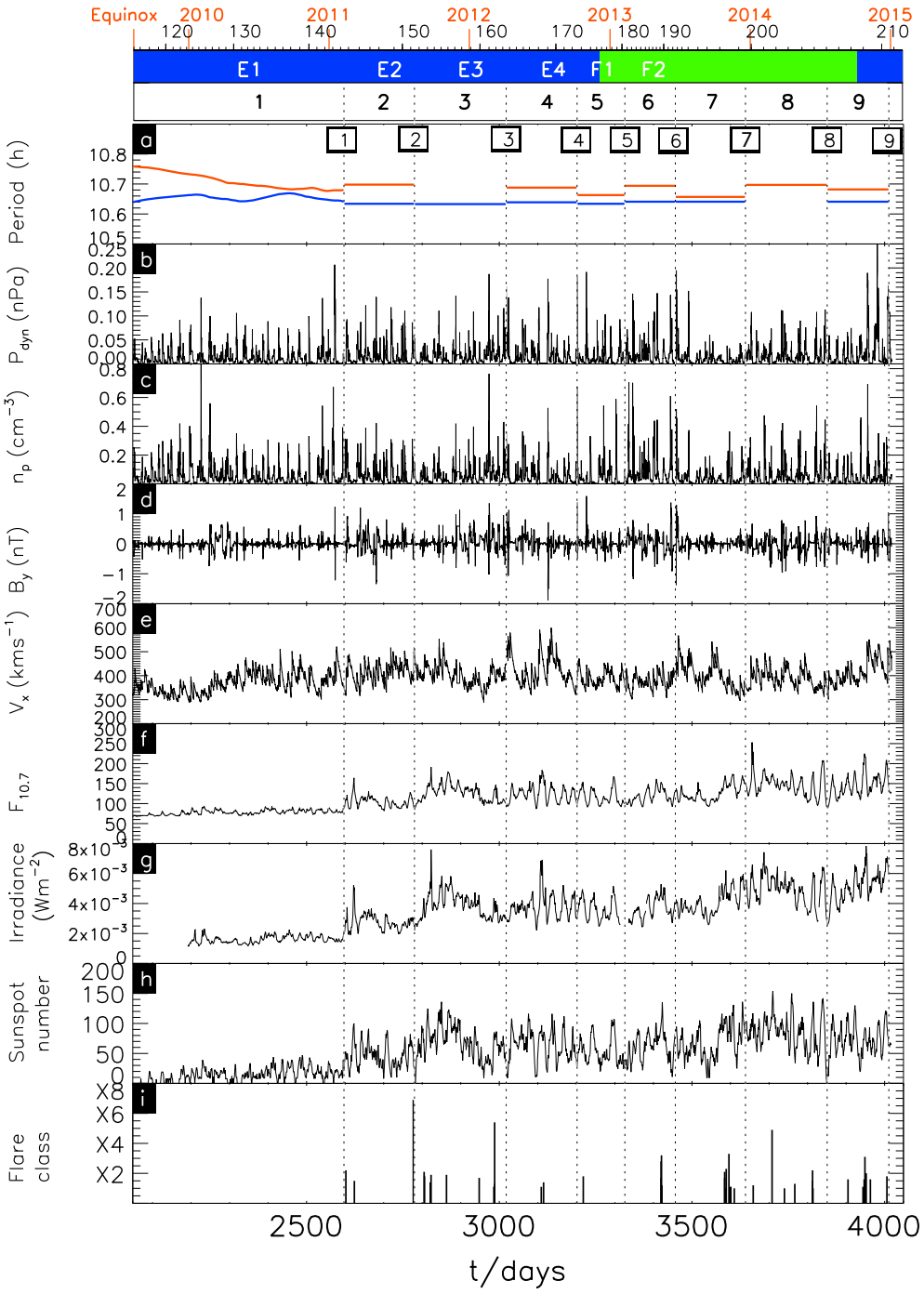

Figure 4. Plots show solar and solar wind data from the equinox at 11 August (2009) ($t = 2049$) to 1 March 2015 ($t = 4077$). Start-of-year and Cassini Rev markers are shown at the top of the plot. The top two bars present the interval identifiers as in Figure 3. Labeled vertical dashed lines mark the times of the nine PPO boundaries. (a) Rotation periods for the southern (red line) and northern (blue) PPOs as in Figure 3b. (b–e) Propagated solar wind data with Figure 4b presenting solar wind dynamic pressure P_{dyn} (nPa), Figure 4c the solar wind proton density n_p (cm^{-3}), Figure 4d the IMF B_y (nT), and Figure 4e the solar wind radial velocity V_x ($km\ s^{-1}$). Solar data below show (f) the daily $F_{10.7}$ index (10.7 cm solar radio flux); (g) the daily mean irradiance from diode 1 from the TIMED/SEE XUV photometer system from ~0.1 to 7 nm; (h) the daily sunspot number, also from the OMNIWEB website; and (i) the time of X-class flares and their classification. For data sources see acknowledgments.

measurements so that only measurements from the spacecraft with the smallest longitudinal separation from Saturn are considered. Figure 4b shows solar wind dynamic pressure, Figure 4c the solar wind proton density, and Figure 4d the *y* component of the interplanetary magnetic field (IMF), B_y, where the *x* axis points radially outward from the Sun in the equatorial plane, the *z* axis points northward, and the *y* axis completes the orthogonal triad. In Tao's propagation model the B_z component of the magnetic field is assumed to be zero and the B_x component small and constant. Figure 4e presents the solar wind velocity in the radial direction, V_x. Figures 4f–4i present solar indices (no time delays have been added to these plots), where Figure 4f presents the daily 10.7 cm solar radio flux index ($F_{10.7}$) from the OMNI website. Figure 4g shows the daily mean irradiance from diode 1 from the TIMED/SEE XUV photometer system from ~0.1 to 7 nm (http://lasp.colorado.edu/lisird/see/level2/2_xps.html). Figure 4h presents the daily sunspot number, as in Figure 2b, also from the OMNI website, and Figure 4i presents the time of X-class flares and their classification from the GOES satellite (ftp://ftp.ngdc.noaa.gov/STP/space-weather/solar-data/solar-features/solar-flares/x-rays/goes/).

Both the solar and the propagated solar wind data presented in Figure 4 show the expected variation over the course of a solar rotation (~27 days). However, this study will primarily focus on longer-term variations in the solar activity as the transitions in PPO behavior have a cadence of ~100–200 days. We note that this is considerably longer than both the 10–30 day SKR variations noted by *Zarka et al*. [2007] and the ~5 day typical cadence of Saturn auroral storms estimated by *Meredith et al*. [2014]. In particular, we will examine whether changes in the PPO behavior are associated with enhanced solar radiation emitted during an unusually powerful solar flare and/or a solar wind disturbance. An example of a solar wind disturbance would be a coronal mass ejection (CME) which triggers an interplanetary shock [see, e.g., *Prangé et al*., 2004; *Prise et al*., 2015]. It is clear that both solar flares and CME often occur together [e.g., *Greenstadt*, 1965], although each can take place in the absence of the other. This can make it difficult to untangle whether it is solar flare or the shock that may be perturbing the PPO characteristic. However, if a flare and a CME occur simultaneously, then their propagation time to Saturn will help identify a possible driver, as solar radiation takes ~80 min to reach Saturn, while an interplanetary shock will take around a month which is the approximate time of a solar rotation [see, e.g., *Prangé et al*., 2004; *Prise et al*., 2015]. This also means that the errors in time associated with predicting the arrival time of a shock are much larger than the errors in determining the arrival time of enhanced solar radiation associated with a solar flare on the same system. Based on the solar wind observations by the Ulysses spacecraft at ~5 AU from the Sun, *Tao et al*. [2005] estimated that the arrival prediction error of the MHD simulation is at most 2 days for an Earth-Sun-observer angle less than 60°. A statistical analysis by *Zieger and Hansen* [2008] of the propagated upstream solar wind data from 1 AU near Earth to 10 AU estimated the accuracy of shock arrival times to be as high as 10–15 h within ±75 days from apparent opposition during years with high recurrence index (so when Earth and the spacecraft were separated by less than ±75° in longitude). The error estimates from *Zieger and Hansen* [2008] and *Tao et al*. [2005] were calculated when they used only one Earth-based solar wind monitor. For this study we use solar wind measurements both from an Earth-based monitor and also from the two STEREO spacecraft, significantly increasing the number of days for which the solar wind monitor is within a conducive narrow angular range of Saturn.

From a visual inspection of Figure 4 we note that there are clear increases in solar indices coinciding with the commencement of the change in PPO behavior (at the time of the first PPO boundary). Below we will present a statistical study of the solar wind and solar conditions associated with the nine boundaries. First, we will present a case study of boundary 3, allowing an abrupt change in PPO behavior and associated solar activity to be examined in detail.

6. Case Study of Boundary 3

Here we present a case study of boundary 3, separating intervals 3 and 4. Boundary 3 occurs between periapsis on Rev 163 ($t = 3008.9$ days) and periapsis on Rev 164 ($t = 3026.71$ days), such that the boundary time is identified as $t = 3017.8 \pm 10$ days (5 April 2012). Interval 3 is the first interval during which the N oscillations are dominant within the equatorial core region ($k \geq 5$), and no S oscillations were detectable within the core region. During interval 4 the N dominance continues but to a lesser extent ($k \approx 1.56$), though both the N and the S oscillations are suppressed at the start of interval 4. The trajectories for these Revs 163 and 164 are almost identical, both being near equatorial, Figure 5 presents the trajectory for Revs 163–165. The orbits are projected onto Saturn's equatorial plane using KSMAG coordinates where the *Z* axis is aligned with Saturn's magnetic and

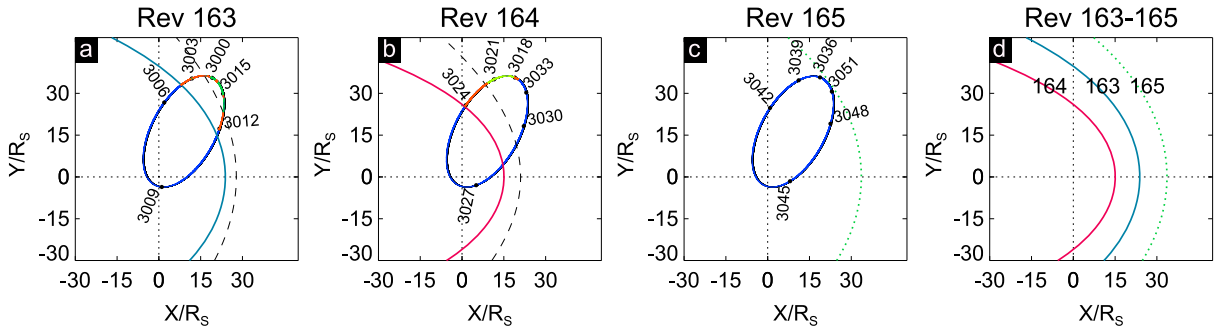

Figure 5. Cassini's trajectory for (a) Rev 163, (b) Rev 164, and (c) Rev 165 projected onto Saturn's equatorial *X-Y* plane in KSMAG coordinates. The orbits are color coded to show the plasma regions observed, namely, the solar wind (green), hot solar wind (light green), magnetosheath (red), and magnetosphere (blue). The position of Cassini at 3 day intervals is shown on the plots with solid black circles, and these times are presented on the plots. Overplotted are related magnetopause locations determined from the model of *Kanani et al.* [2010] and the bow shock location from *Masters et al.* [2008]. Specifically, in Figure 5a the blue line shows the magnetopause boundary for $P_{dyn} = 0.015$ nPa while the dashed black line shows the bow shock location for $P_{dyn} = 0.03$ nPa. In Figure 5b the pink line shows the magnetopause location for $P_{dyn} = 0.15$ nPa, while the dashed black line shows the bow shock location for $P_{dyn} = 0.1$ nPa. In Figure 5c the magnetopause boundary is presented as a dotted green line at its minimum possible standoff distance for $P_{dyn} = 0.0027$ nPa. (d) A summary of the position of the magnetopause boundaries during Revs 163–165 for $P_{dyn} = 0.015$ nPa Rev 163 (blue), $P_{dyn} = 0.15$ nPa Rev 164 (pink), and $P_{dyn} = 0.0027$ nPa Rev 165 (green).

rotational axis, the *X*-Z plane contains the Sun, and *Y* completes the right-hand set. Revs 163–165 are near-equatorial Revs, and so we only present the orbit trajectory in the *X-Y* plane. The trajectories are color coded to show different regions identified on the basis of Cassini Plasma Spectrometer/electron spectrometer (CAPS/ELS) plasma electron data and magnetic field data, where green corresponds to the solar wind, light green to "hot solar wind," red to the magnetosheath, and blue to the magnetosphere. Modeled magnetopause boundaries [*Kanani et al.*, 2010], congruent to the observed locations, are overplotted as a solid blue line in Figure 5a, a solid pink line in Figure 5b, and a dotted green line in Figure 5c, with all three boundaries being presented in Figure 5d. Modeled bow shock locations [*Masters et al.*, 2008] are overplotted in Figures 5a and 5b with dashed black lines. The identification of the different plasma regimes and magnetopause and bow shock boundaries are described below.

Figure 6 presents Cassini data from a few days prior to periapsis on Rev 163 to a few days after periapsis on Rev 164. The two periapses are labeled at the top of the plot. Figure 6a shows the electron spectrogram color coded according to the scale on the right covering the energy range 0.6 eV to 28 keV obtained by the ELS sensor of the Cassini Plasma Spectrometer [*Young et al.*, 2004]. Figures 6b–6g show magnetic field data obtained by the Cassini fluxgate magnetometer [*Dougherty et al.*, 2004], specifically three pairs of panels showing residual and filtered data for each of the radial (r), colatitudinal (θ), and azimuthal (φ) spherical polar field components referenced to Saturn's spin and magnetic axis. The upper panel of each pair shows 1 min residual field data with the internal field of the planet subtracted using the "Cassini SOI" model [*Dougherty et al.*, 2005]. The lower panel of each pair shows the filtered residual data, where we have used band-pass filters between periods of 5 and 20 h. It is from the ELS data, in conjunction with the magnetic field data, that we have identified the different plasma regimes. These regimes are color coded in the bar at the top of the plot using the same region identifiers introduced for Figure 5. The solid black lines demark the two intervals of observations from Saturn's core magnetosphere from which core phases were determined for Rev 163 and Rev 164, as shown in Figure 3.

Rev 163 demonstrates the strong northern dominance of the oscillations, with the r and θ components in antiphase and the r component in leading quadrature with the φ component. Rev 164 is then very unusual in showing only small oscillations to be present in all three field components. As a consequence, the phase data in all three components are deemed to be unreliable, as described by *Provan et al.* [2013]. Clearly, the change in PPO behavior occurs between periapsis on Rev 163 and periapsis on Rev 164, such that at the time boundary 3 is defined as $t = 3017.8$ days (5 April 2012), which is the midtime between these two periapses.

In order to gain a greater understanding of the magnetospheric, solar and solar wind conditions associated with this change in behavior, Figure 7 presents data from the start of Rev 162 to the end of Rev 165. Figure 7a presents the CAPS/ELS data, while Figures 7b–7g show the residual and the filtered residual magnetic field data for the r (Figures 7b and 7c), θ (Figures 7d and 7e), and φ (Figures 7f and 7g) components. Figure 7h presents the solar wind dynamic pressure which has been propagated to Saturn as described in section 5,

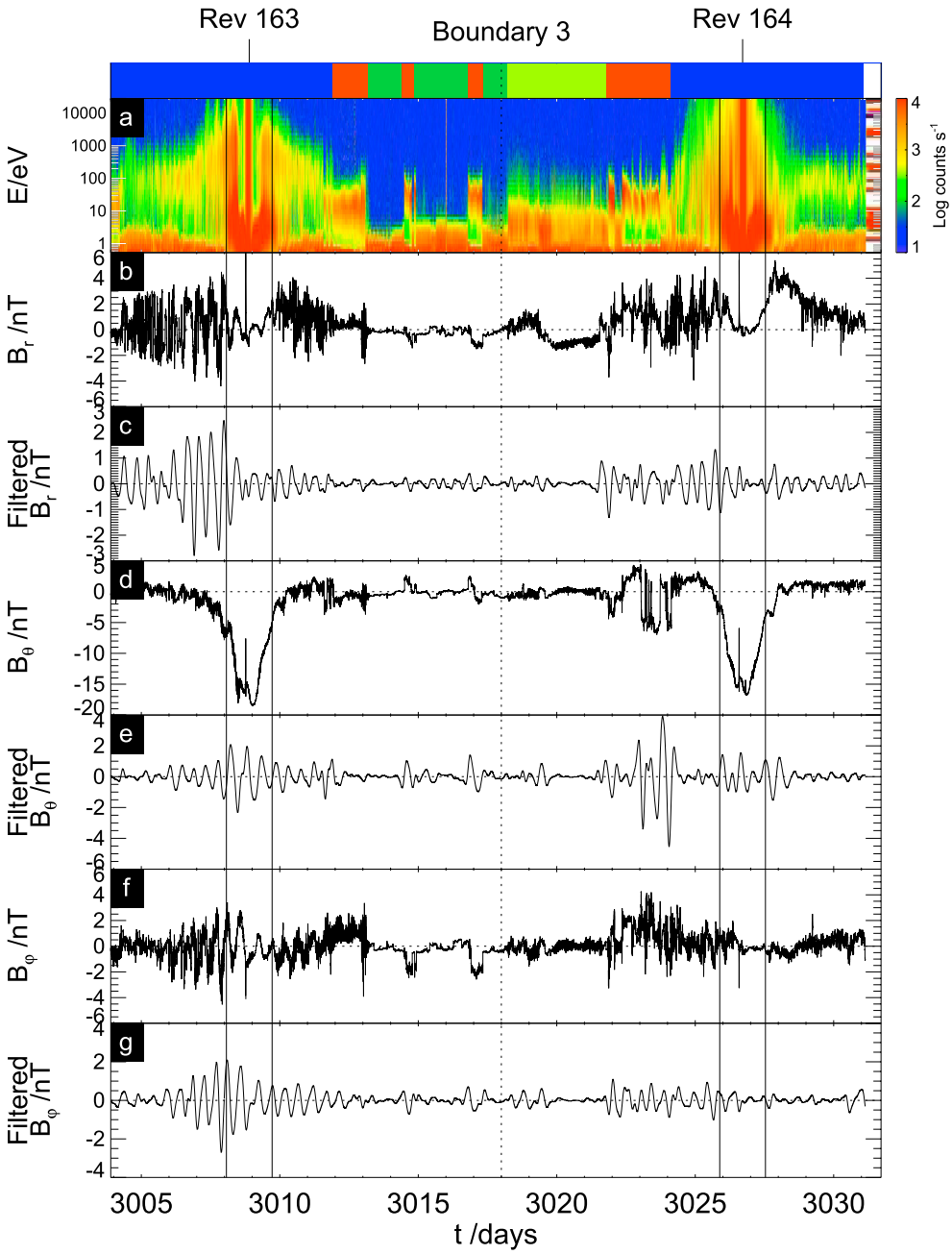

Figure 6. Plot of Cassini plasma electron and magnetic field data from 5 days prior to periapsis for Rev 163 (22 March 2012, $t = 3003$ days) to 5 days after periapsis on Rev 164 (19 April 2012, $t = 3031$ days). The two periapses are labeled at the top of the plot. The top bar indicates the different plasma regimes, color coded as in Figure 5. (a) Electron spectrogram color coded according to the scale on the right and (b–g) three pairs of magnetic field data panels for the radial (r), colatitudinal (θ), and azimuthal (φ) spherical polar field components referenced to the planet's spin and magnetic axis (nT). The upper panel in each pair shows the residual field component with the Cassini SOI model of the planetary field subtracted, while the lower panel shows this residual component band pass filtered between periods of 5 and 20 h. The solid vertical black lines demark the two intervals of data from Saturn's core magnetosphere (dipole $L < 12\ R_S$) for Revs 163 and 164 whose analysis yields the core phases for these two Revs. The dashed black line indicates the time of boundary 3.

while Figure 7i shows the daily mean irradiance in XUV from TIMED, as in Figures 4b and 4g, respectively. The top bar identifies the different plasma regimes, in the same format as Figures 5 and 6. At $t \sim 3018$ days Cassini abruptly starts to observe hot solar wind, suggestive of a solar wind disturbances reaching Saturn's magnetopause boundary. Figure 7h demonstrates that between periapsis on Rev 163 and periapsis on Rev 164 there

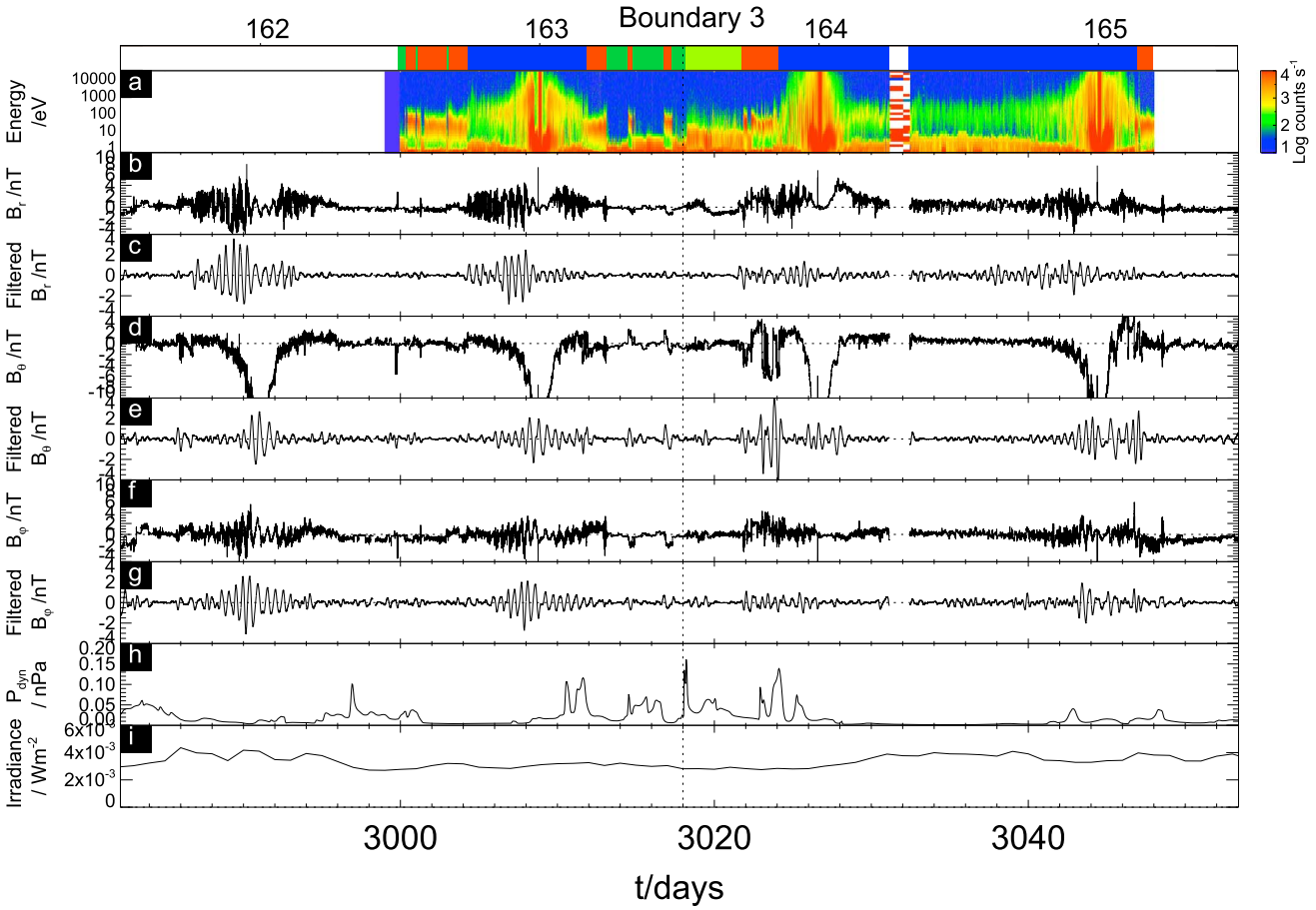

Figure 7. (a–g) Cassini plasma electron and magnetic field data as in Figure 6, here from the start of Rev 162 (1 March 2012, $t = 2982$ days) to the end of Rev 165 (11 May 2012, $t = 3053$ days). The top bar shows the different plasma regimes, color coded as in Figures 5 and 6. (h and i) The propagated solar wind dynamic pressure and the daily mean irradiance in XUV. The dashed black and white line demarks the time of boundary 3.

are four clear peaks in the predicted solar wind dynamic pressure signaling the arrival of four solar wind compression events at Saturn's magnetopause. After the fourth compression event the solar wind dynamic pressure falls to extremely low values.

Saturn and Earth were in opposition on $t = 3027$ days (15 April 2012); hence, any interplanetary shock should successively encounter Earth and then Saturn when propagating radially outward. *Prangé et al.* [2004] presented a case study of an interplanetary shock propagation which took approximately a month to propagate from the Sun to Saturn at a time of opposition (i.e., propagating ~10 AU at ~600 km s^{-1}). It was reported (for example, in the NOAA weekly report http://www.swpc.noaa.gov/) that four large flares were observed between $t = 2986$ and 2991 days (5–10 March 2012), and all four flares were associated with earthward directed CMEs. One of the four flares was a massive 5.4 X-ray flare which occurred on $t = 2988$ days (7 March 2012), as also presented in Figure 4i. These are likely the four solar wind compressions that are predicted to arrive at Saturn between the periapsis of Rev 163 and the periapsis of Rev 164.

In Figure 8 we explore these large flares, in particular the 5.4 X-ray flare, and demonstrate how these impinge on the Saturnian environment. Figure 8a shows solar flare activity observed on $t = 2988$ days (7 March 2012) by the SWAP EUV telescope on board the PROBA2 spacecraft (http://proba2.oma.be/data/SWAP) [*Seaton et al.*, 2013]. PROBA2 is in a Sun-synchronous Earth orbit. Figure 8b shows the GOES X-ray flux from $t = 2984$–2991 days (3 to 10 March 2012). The GOES satellites are in geosynchronous orbits and provide measurements of solar X-rays in the 0.1–0.8 nm and 0.05–0.4 nm passbands (http://www.swpc.noaa.gov/products/goes-x-ray-flux). The GOES data were plotted using the website http://www.polarlicht-vorhersage.de/goes_archive. The four large flares are clearly visible in the data. Figure 8c presents the location of the Sun, the Earth (green circle),

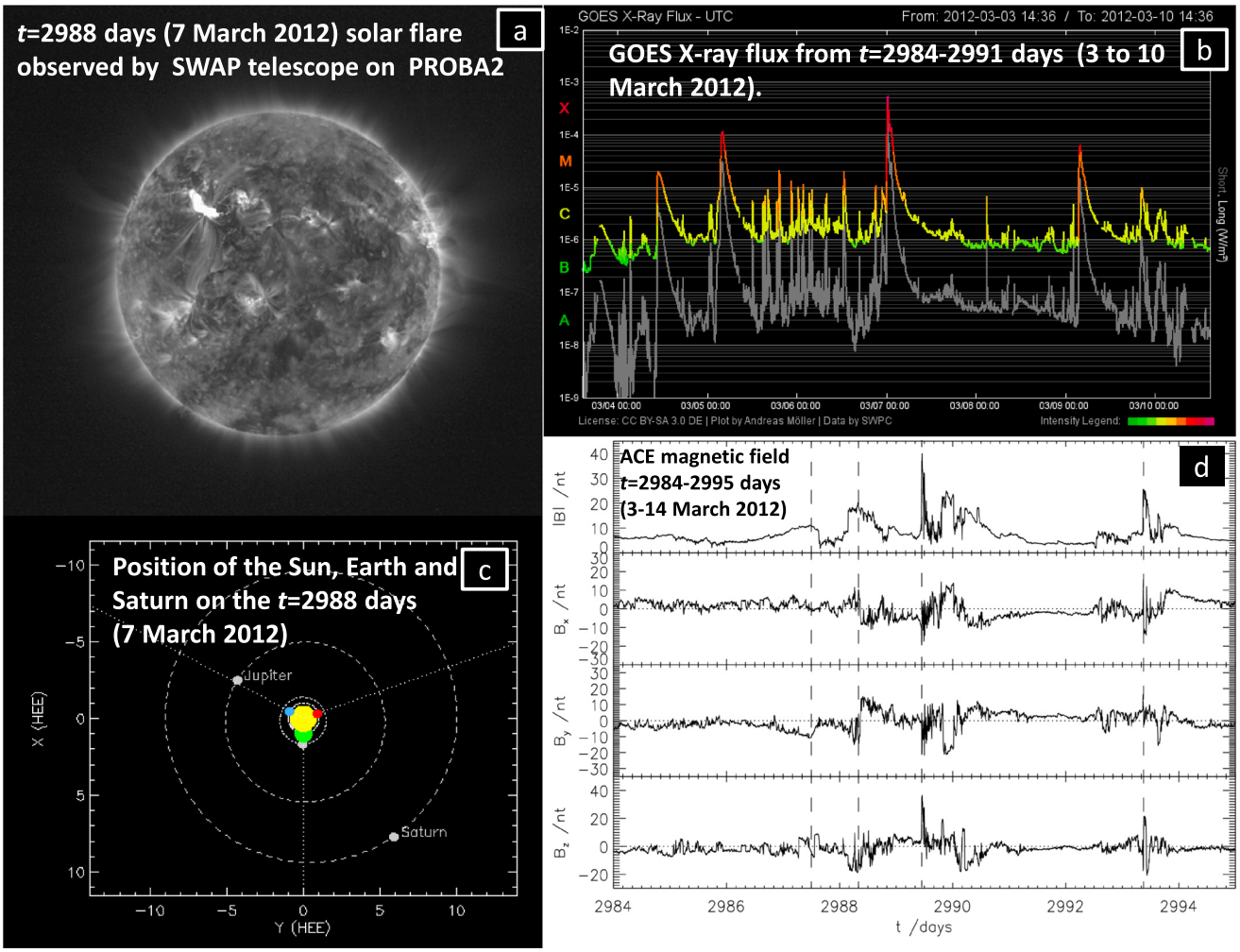

Figure 8. (a) Solar flare activity observed on 7 March 2012 ($t = 2988$ days) by the SWAP telescope on board the PROBA2 spacecraft in Sun-synchronous orbit around Earth; (b) the GOES X-ray flux from 3 to 10 March 2012 ($t = 2984$–2991 days); (c) the location of the Sun, the Earth (green circle), the STEREO spacecraft (red and blue circles), and Jupiter and Saturn in the *X-Y* helio-ecliptic plane on 7 March 2012 ($t = 2988$) from STEREO Science Center (http://stereo-ssc.nascom.nasa.gov/where.shtml); and (d) the magnetic field measurements from 3 to 14 March 2012 ($t = 2984$–2995) from the ACE spacecraft at the L1 Lagrange point. The approximate times of the four CMEs are identified on the plot with dashed black lines.

the STEREO spacecraft (red and blue circles), and Jupiter and Saturn in the *X-Y* helio-ecliptic plane on $t = 2988$ days (7 March 2012) plotted using http://stereo-ssc.nascom.nasa.gov/where.shtml. Earth and Saturn are separated by ~38° on this day (with their angular separation ranging from ~42° to ~35° from 3 to 10 March 2012). Figure 8d presents the ACE magnetic field measurements from $t = 2984$–2995 days (3 to 14 March 2012); the succession of four CMEs is clearly observable in the magnetic field data, and their approximate times are identified on the plot with dashed black lines.

The four solar wind compressions that are predicted to arrive at Saturn between the periapsis of Rev 163 and the periapsis of Rev 164 occur contemporaneously with a marked reduction in the size of Saturn's magnetosphere. The trajectory data that are presented in Figure 5 are color coded to show the various magnetospheric regions. We also show the modeled magnetopause [*Kanani et al.*, 2010] and bow shock [*Masters et al.*, 2008] boundaries. The magnetopause boundaries are presented in blue for Rev 163, pink for Rev 164, and green for Rev 165. The magnetopause boundary for Rev 163 corresponds to a dynamic pressure of $P_{dyn} = 0.015$ nPa, corresponding to the magnetopause location observed both on Rev 163 inbound and Rev 163 outbound. The position of the bow shock corresponds to $P_{dyn} = 0.03$ nPa. For Rev 164 both the magnetopause and the bow shock boundaries have moved sharply inward, demonstrating a significant compression of the Saturn's magnetosphere. This is observed contemporaneously with the four high dynamic

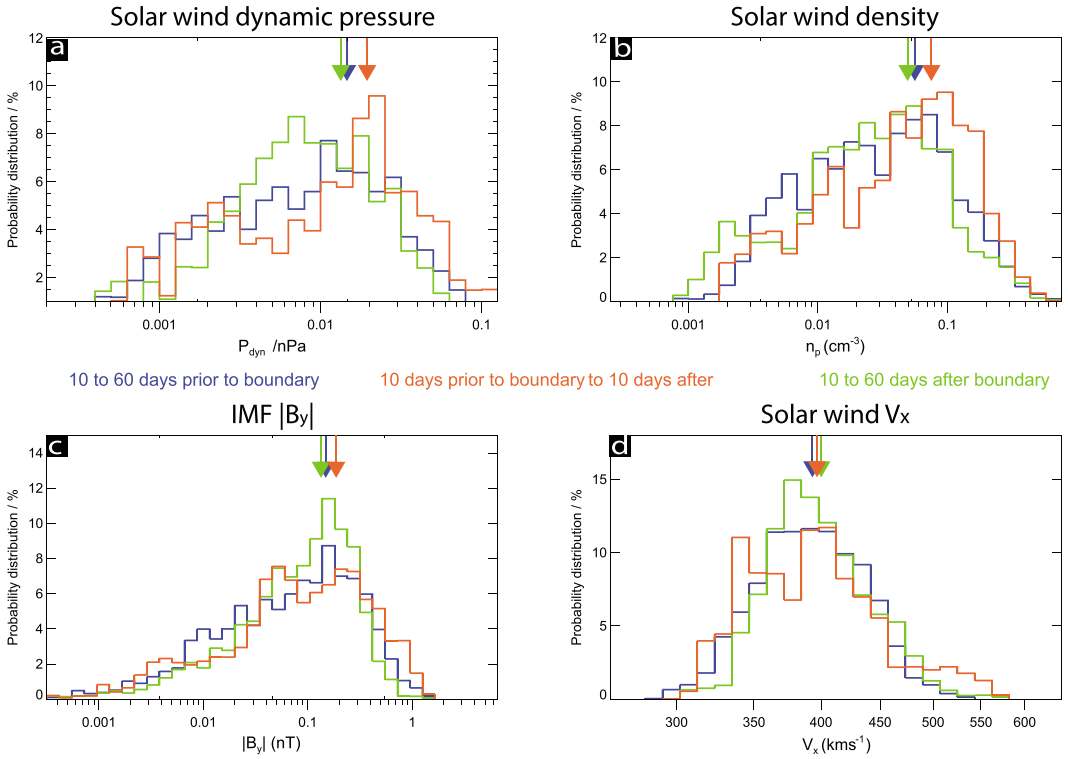

Figure 9. Percentage occurrence histograms of (a) solar wind dynamic pressure, (b) solar wind density, (c) IMF $|B_y|$, and (d) solar wind V_X for eight PPO boundaries for three separate time intervals spanning 10–60 days before the PPO boundary (blue line), 10 days before to 10 days after the PPO boundary (red line), and 10–60 days after the boundary (green line). The mean value of the data within each interval is indicated by a color-coded arrow in the top of the plot. The parameters are shown on a log scale with log spaced data bins.

pressure events arriving at Saturn. The magnetopause boundary is consistent with $P_{dyn} = 0.15$ nPa, while the bow shock location is calculated for $P_{dyn} = 0.1$ nPa. The peak-propagated solar wind dynamic pressure for Rev 164 is $P_{dyn} = 0.16$ nPa. After periapsis on Rev 164 the propagated solar wind dynamic pressure falls to very low levels. It can be seen that Saturn's magnetosphere expands sharply with Cassini remaining within the magnetosphere throughout the 164/165 apoapses. In Figure 5c the position of the magnetopause during Rev 165 is shown at its minimum standoff distance consistent with $P_{dyn} < 0.0027$ nPa, drawn as a dotted line. Figure 5d presents a summary of the position of the magnetopause boundaries during Revs 163–165, showing how the standoff distance of the subsolar magnetopause varies by at least 15 R_s between Rev 163 and Rev 165 as Saturn's magnetosphere first rapidly contracts and then expands.

In conclusion, boundary 3 occurs at a time of rapid and significant changes in the size of Saturn's magnetosphere, observed contemporaneously with the arrival of solar wind compressions and expansions at Saturn's magnetopause. In the following section we will present a statistical study to examine whether this may be more generally the case over all the PPO boundaries examined in this study.

7. Statistical Study

We have performed a superposed epoch analysis on the propagated solar wind data from 2 months prior to each PPO boundary until 2 months after. Unfortunately, because boundary 9 occurred on the $t = 4010.8$ days (24 December 2014), and we only have propagated solar wind data up to the end of 2014, boundary 9 has not been included in this analysis. For each of the remaining eight boundaries the solar wind data have been divided into three separate intervals (a) from 60 to 10 days prior to each boundary, (b) from 10 days prior to each boundary to 10 days after, and (c) from 10 to 60 days after each boundary. Considering the solar wind conditions over a 20 day period centered on a PPO boundary allows for the uncertainties associated with identifying the boundary times. As these times are defined as the midpoint between two periapses which

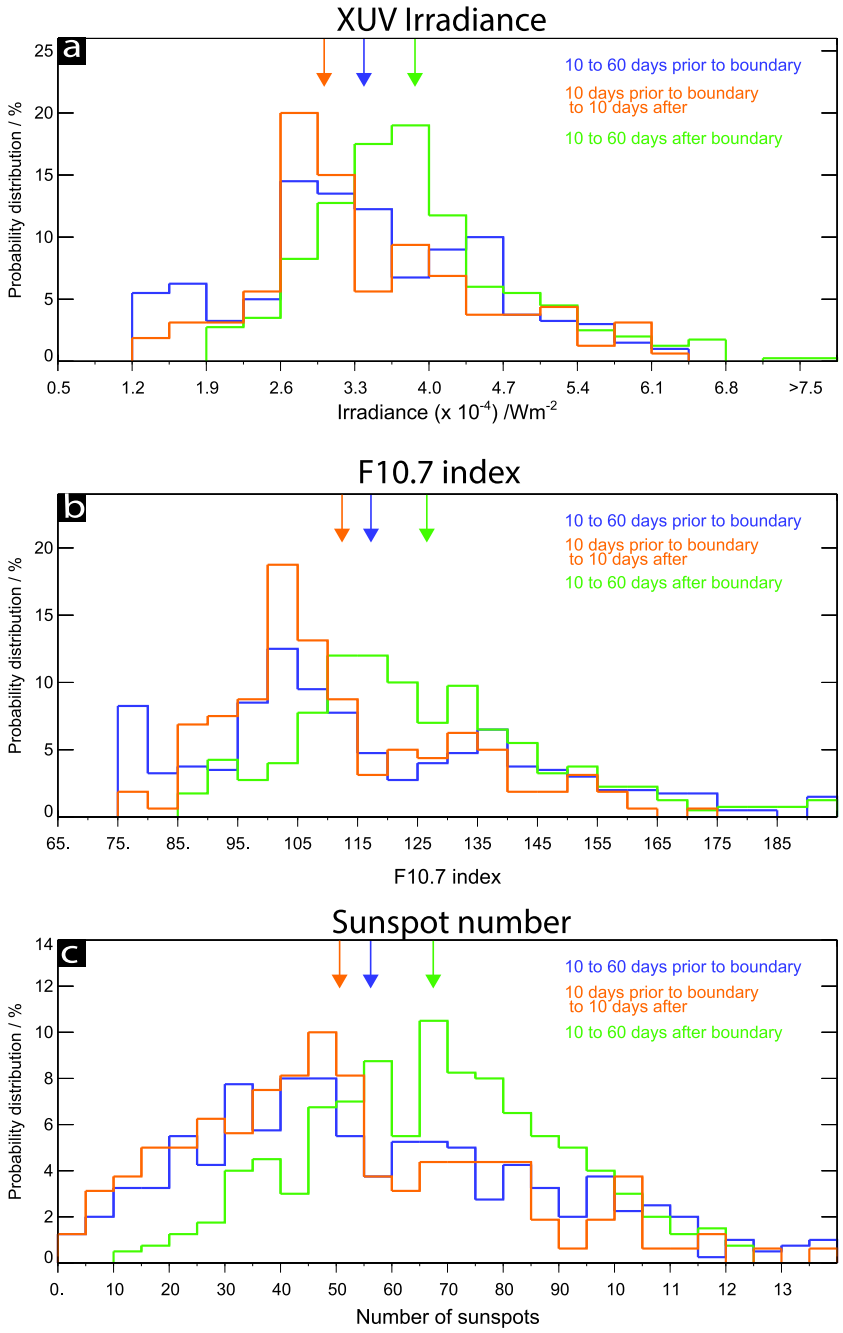

Figure 10. Percentage occurrence histograms of (a) the total XUV solar irradiance, (b) the $F_{10.7}$ index, and (c) the sunspot number for the PPO boundaries 1–8. The format is similar to Figure 9, although here each parameter is shown on a linear scale with linearly spaced data bins.

are separated by ~20 days, their uncertainty is ±10 days. Considering intervals of 60 days on either side of a particular boundary generally means that it will not include related conditions around adjacent boundaries, such that the data for each are separated.

Figure 9 presents normalized histograms showing the percentage distributions of (a) solar wind dynamic pressure, (b) solar wind density, (c) IMF $|B_y|$, and (d) solar wind V_x for the three time intervals. The data are presented on a logarithmic scale with log space data bins. Data observed 10 to 60 days before each boundary are shown in blue, data observed 10 days prior to 10 days after each boundary are shown in red, and data observed 10–60 days after each boundary are shown in green. The mean value of the data for each binned

time interval is indicated by a color-coded arrow at the top of the plot. Inspection of Figure 9 clearly demonstrates that the histograms for the solar wind dynamic pressure, solar wind density, and IMF $|B_y|$ are displaced toward larger values for the days centered on the PPO boundaries, as opposed to the data observed before or after each boundary. This is also clearly indicated by the mean values of the parameters. Figure 9d demonstrates that the solar wind velocity, V_x, has very similar distributions and mean values before, during, and after the boundaries. Thus, solar wind density, rather than the solar wind velocity, appears to be the key parameter in enhancing the solar wind dynamic pressure during the PPO boundaries.

Figure 10 presents a similar analysis performed for the solar indices shown in Figure 4. We present percentage occurrence histograms of (a) the XUV irradiance, (b) $F_{10.7}$ index, and (c) sunspot number. Here the data are presented on a linear scale. The solar indices observed during the PPO boundaries do not present a markedly different behavior in comparison to the solar indices observed 60–10 days before the boundaries. However, all three indices are enhanced after the PPO boundaries. This might indicate an increase in solar activity prior to a forthcoming PPO boundary. All in all, the solar wind events associated with the PPO boundaries revealed by the case study in section 6 and the superposed epoch study presented here thus appear to be initiated in the ~30 day propagation interval prior to the emergence of new solar active regions that give rise to enhancements in the X-ray and radio flux and sunspot numbers in the following interval, as can be seen to be often, if not invariably, the case in Figure 4.

8. Summary and Conclusions

In this paper we have studied abrupt changes in the behavior of the PPOs identified in the postequinox interval. We have presented evidence that the amplitudes and periods of the PPOs are, at least in part, controlled by conditions external to the Saturnian system by demonstrating that the sharp change in their characteristics appears to be associated with abrupt variations in the size of the Saturian magnetosphere associated with the arrival of interplanetary shocks at Saturn's magnetosphere. Further, we report that while such modulations in PPO behavior are associated with enhanced values of solar wind dynamic pressure and solar wind density, they are not associated with discernibly enhanced values of solar wind speed, indicating that the solar wind density appears to be the key parameter in influencing changes in PPO behavior. We further report that all three indices of solar activity considered in this paper, sunspot number, XUV radiation, and the $F_{10.7}$ index, show similar values before and during the PPO boundaries but demonstrate enhanced values in the interval 10–60 days after the PPO boundaries. The PPO boundaries are separated ~100–200 days. It therefore seems likely that this enhanced solar activity heralds the emergence of new solar active region, resulting in the enhanced solar wind density and dynamic pressure which are observed during the PPO boundaries.

There have been previous reports of correlations between variations in SKR period and power with solar wind parameters. *Zarka et al.* [2007] reported a correlation between short-term (<1 month) variations in SKR period with solar wind velocity and suggested a probable similar relationship for longer-term (>1 month) variations. *Desch and Rucker* [1983, 1985] reported a strong relationship between solar wind density and emitted SKR power. However, this report was concerned with variations with cadence of ~5–10 days which is the typical cadence of Saturn auroral storms estimated by *Meredith et al.* [2014]. The observations of *Zarka et al.* [2007] were made during the declining phase of the solar cycle when the solar wind had a high recurrence index due to the prevalence of corotating interacting regions. The study by *Desch and Rucker* [1983] and the one presented here were both performed during a time of increased solar activity when CMEs would be prevalent in the solar wind. Our results demonstrate the importance of taking into account the nature of the solar wind on solar cycle timescales when considering the relationship between the solar wind and the Saturnian magnetosphere.

Next, we will consider how changes in solar wind density may be affecting the PPOs. *Hunt et al.* [2014] have reported PPO modulations of the southern hemisphere field-aligned current system. Further work by *Hunt et al.* [2015] provided the first evidence of interhemispheric PPO-related field-aligned currents, as previously suggested by *Southwood and Kivelson* [2007]. *Badman et al.* [2015] reported a solar wind compression impacting on Saturn's magnetosphere, describing an enhancement in the northern hemisphere field-aligned currents at the time of this solar wind compression. The results presented in this paper raise the possibility that the field-aligned currents are modified by the expansion and contraction of the Saturnian magnetosphere in response to solar wind compressions and expansions—resulting in modification in the amplitudes and the periods of the PPOs.

This paper suggests several new avenues of further research. The first is that although we present evidence that the solar wind density is associated with changes in the behavior of the PPOs, it is clear from Figure 4 that not all increases in density are related to changes in the behavior of the PPOs. It is possible that since we are propagating the solar wind over 10 AU, there are times when the model does not fully reflect the behavior of the solar wind at Saturn. It is also likely that a second unknown parameter is involved that also influences how susceptible Saturn's PPOs are to modulation of the solar wind density. It is undoubtedly true that Saturn's magnetospheric dynamics is influenced by several different drivers. *Kimura et al*. [2013] suggested that at Saturn solar wind variations on solar cycle timescale affect the long-term magnetosphere-ionosphere coupling process on top of the baseline of the seasonal variations. This would seem to agree with the results presented here where we have observed a seasonal cause of the north-south asymmetry in the PPO periods seemingly associated with solar illumination and the abrupt changes in PPO behavior associated solar wind compressions and expansions. Interplay between different drivers may explain the previous results of *Provan et al*. [2013], who reported that while postequinox PPO transitions occur simultaneously in the two hemispheres, they often result in variations that are in antiphase in the two hemispheres, especially for the amplitude variations. For example, at boundary 1 the southern amplitude and period increase while the northern amplitude and period decrease. At boundary 2 the southern amplitude decreases sharply while the northern amplitude increases. Interestingly, at boundary 3 both the northern and the southern amplitudes are initially suppressed. As these abrupt changes are related to large-scale variation in the size of the Saturnian magnetosphere, this begs the question as to why such a seemingly global Saturnian event does not consistently lead to changes in PPOs behavior that are in phase between the two hemispheres, e.g., the amplitudes of the PPO oscillations increasing or decreasing simultaneously in both the northern and southern hemispheres. Seasonal variations in Saturn's atmosphere between the planet's two hemispheres may be one possible explanation for such antiphase responses and will be an avenue for further research.

Acknowledgments

Work at the University of Leicester was supported by STFC grant ST/K001000/1. We thank S. Kellock and the Cassini Mag team at Imperial College for access to processed magnetic field data. Calibrated magnetic field and radio data from the Cassini mission are available from the NASA Planetary Data System at the Jet Propulsion Laboratory (https://pds.jpl.nasa.gov/). TIMED/SEE XUV photometer systems were obtained from LASP (http://lasp.colorado.edu/lisird/see/level2/2_xps.html). X-ray fluxes are available from the GOES satellites (ftp://ftp.ngdc.noaa.gov/STP/space-weather/solar-data/solar-features/solar-flares/x-rays/goes/). The $F_{10.7}$ index and the sunspot numbers were downloaded from Goddard Space Flight Center Space Physics Data Facility OMNIWEB (http://omniweb.gsfc.nasa.gov/form/dx1.html). The position of the STEREO spacecraft has been provided by the STEREO Science Center (http://stereo-ssc.nascom.nasa.gov/where.shtml). The GOES X-ray flux plotting tool was provided by Andreas Möller (http://www.polarlicht-vorhersage.de/goes_archive/). ACE magnetic field data are available from CDAWeb (http://cdaweb.gsfc.nasa.gov/cgi-bin/eval3.cgi). Swap images from the PROBA2 spacecraft are available from http://proba2.oma.be/about/SWAP. SWAP is a project of the Centre Spatial de Liege and the Royal Observatory of Belgium funded by the Belgian Federal Science Policy Office (BELSPO). The authors would like to thank J. Janssens from the Solar Influences Data Analysis Center in Belgium for the useful discussions on the solar data. Propagated solar wind data are available from C. Tao by private correspondence (chihiro.tao@irap.omp.eu). Propagated solar wind data from OMNI are available at AMDA (http://amda.cdpp.eu).

References

Andrews, D. J., E. J. Bunce, S. W. H. Cowley, M. K. Dougherty, G. Provan, and D. J. Southwood (2008), Planetary period oscillations in Saturn's magnetosphere: Phase relation of equatorial magnetic field oscillations and SKR modulation, *J. Geophys. Res.*, *113*, A09205, doi:10.1029/2007JA012937.

Andrews, D. J., S. W. H. Cowley, M. K. Dougherty, and G. Provan (2010a), Magnetic field oscillations near the planetary period in Saturn's equatorial magnetosphere: Variation of amplitude and phase with radial distance and local time, *J. Geophys. Res.*, *115*, A04212, doi:10.1029/2007JA014729.

Andrews, D. J., A. J. Coates, S. W. H. Cowley, M. K. Dougherty, L. Lamy, G. Provan, and P. Zarka (2010b), Magnetospheric period oscillations at Saturn: Comparison of equatorial and high-latitude magnetic field periods with north and south SKR periods, *J. Geophys. Res.*, *115*, A12252, doi:10.1029/2010JA015666.

Andrews, D. J., S. W. H. Cowley, M. K. Dougherty, L. Lamy, G. Provan, and D. J. Southwood (2012), Planetary period oscillations in Saturn's magnetosphere: Evolution of magnetic oscillation properties from southern summer to post-equinox, *J. Geophys. Res.*, *117*, A04224, doi:10.1029/2011JA017444.

Badman, S. V., S. W. Cowley, L. Lamy, B. Cecconi, and P. Zarka (2008), Relationship between solar wind corotating interaction regions and the phasing and intensity of Saturn kilometric radiations bursts, *Ann. Geophys.*, *26*, 3641–3651.

Badman, S. V., et al. (2012), Rotational modulation and local time dependence of Saturn's infrared H_3^+ auroral intensity, *J. Geophys. Res.*, *117*, A09228, doi:10.1029/2012JA017990.

Badman, S. V., et al. (2015), Saturn's auroral morphology and field-aligned currents during a solar wind compression, *Icarus*, doi:10.1016/j.icarus.2014.11.014, in press.

Burch, J. L., A. D. DeJong, J. Goldstein, and D. T. Young (2009), Periodicity in Saturn's magnetosphere: Plasma cam, *Geophys. Res. Lett.*, *36*, L14203, doi:10.1029/2009GL039043.

Burton, M. E., M. K. Dougherty, and C. T. Russell (2010), Saturn's internal planetary magnetic field, *Geophys. Res. Lett.*, *37*, L24105, doi:10.1029/2010GL045148.

Carbary, J. F., and S. M. Krimigis (1982), Charged particle periodicity in the Saturnian magnetosphere, *Geophys. Res. Lett.*, *9*, 1073–1076, doi:10.1029/GL009i009p01073.

Carbary, J. F., D. G. Mitchell, S. M. Krimigis, and N. Krupp (2007), Electron periodicities in Saturn's outer magnetosphere, *J. Geophys. Res.*, *112*, A03206, doi:10.1029/2006JA012077.

Carbary, J. F., D. G. Mitchell, P. Brandt, C. Paranicas, and S. M. Krimigis (2008a), ENA periodicities at Saturn, *Geophys. Res. Lett.*, *35*, L07102, doi:10.1029/2008GL033230.

Carbary, J. F., D. G. Mitchell, P. Brandt, E. C. Roelof, and S. M. Krimigis (2008b), Periodic tilting of Saturn's plasma sheet, *Geophys. Res. Lett.*, *35*, L24101, doi:10.1029/2008GL036339.

Cecconi, B., and P. Zarka (2005), Model of a variable radio period for Saturn, *J. Geophys. Res.*, *110*, A12203, doi:10.1029/2005JA011085.

Clarke, K. E., et al. (2006), Cassini observations of planetary-period oscillations of Saturn's magnetopause, *Geophys. Res. Lett.*, *33*, L23104, doi:10.1029/2006GL027821.

Cowley, S. W. H., D. M. Wright, E. J. Bunce, A. C. Carter, M. K. Dougherty, G. Giampieri, J. D. Nichols, and T. R. Robinson (2006), Cassini observations of planetary-period magnetic field oscillations in Saturn's magnetosphere: Doppler shifts and phase motion, *Geophys. Res. Lett.*, *33*, L07104, doi:10.1029/2005GL025522.

Davies, M. E., V. K. Abalakin, J. H. Lieske, P. K. Seidelmann, A. T. Sinclair, A. M. Sinzi, B. A. Smith, and Y. S. Tjuflin (1983), Report of the IAU Working Group on Cartographic Coordinates and Rotational Elements of the Planets and Satellites: 1982, *Celestial Mech.*, *29*, 309–321.

Desch, M. D. (1982), Evidence for solar wind control of Saturn radio emission, *J. Geophys. Res.*, *87*, 4549–4554, doi:10.1029/JA087iA06p04549.
Desch, M. D., and M. L. Kaiser (1981), Voyager measurement of the rotation period of Saturn's magnetic field, *Geophys. Res. Lett.*, *8*, 253–256, doi:10.1029/GL008i003p00253.
Desch, M. D., and H. O. Rucker (1983), The relationship between Saturn kilometric radiation and the solar wind, *J. Geophys. Res.*, *88*, 8999–9006, doi:10.1029/JA088iA11p08999.
Desch, M. D., and H. O. Rucker (1985), Saturn radio emissions and the solar wind: Voyager-2 studies, *Adv. Space Res.*, *15*(4), 333–336.
Dougherty, M. K., et al. (2004), The Cassini magnetic field investigation, *Space Sci. Rev.*, *114*, 331–383, doi:10.1007/s11214-004-1432-2.
Dougherty, M. K., et al. (2005), Cassini magnetometer observations during Saturn orbit insertion, *Science*, *307*, 1266–1270.
Espinosa, S. A., and M. K. Dougherty (2000), Periodic perturbations in Saturns magnetic field, *Geophys. Res. Lett.*, *27*, 2785–2788, doi:10.1029/2000GL000048.
Galopeau, P. H. M., and A. Lecacheux (2000), Variations of Saturn's radio rotation period measured at kilometer wavelengths, *J. Geophys. Res.*, *105*, 13,089–13,101, doi:10.1029/1999JA005089.
Greenstadt, E. W. (1965), Interplanetary magnetic effects of solar flares: Explorer 18 and Pioneer 5, *J. Geophys. Res.*, *70*, 5451–5452, doi:10.1029/JZ070i021p05451.
Gurnett, D. A., W. S. Kurth, and F. L. Scarf (1981), Plasma waves near Saturn: Initial results from Voyager 1, *Science*, *212*, 235–239.
Gurnett, D. A., et al. (2005), Radio and plasma wave observations at Saturn from Cassini's approach and first orbit, *Science*, *307*, 1255–1259.
Gurnett, D. A., A. M. Persoon, W. S. Kurth, J. B. Groene, T. F. Averkamp, M. K. Dougherty, and D. J. Southwood (2007), The variable rotation period of the inner region of Saturn's plasma disk, *Science*, *316*, 442–445, doi:10.1126/science.1138562.
Gurnett, D. A., A. Lecacheux, W. S. Kurth, A. M. Persoon, J. B. Groene, L. Lamy, P. Zarka, and J. F. Carbary (2009a), Discovery of a north-south asymmetry in Saturn's radio rotation period, *Geophys. Res. Lett.*, *36*, L16102, doi:10.1029/2009GL039621.
Gurnett, D. A., A. M. Persoon, J. B. Groene, A. J. Kopf, G. B. Hospodarsky, and W. S. Kurth (2009b), A north-south difference in the rotation rate of auroral hiss at Saturn: Comparison to Saturn's kilometric radio emission, *Geophys. Res. Lett.*, *36*, L21108, doi:10.1029/2009GL040774.
Gurnett, D. A., et al. (2010a), A plasmapause-like density boundary at high latitudes in Saturn's magnetosphere, *Geophys. Res. Lett.*, *37*, L16806, doi:10.1029/2010GL044466.
Gurnett, D. A., J. B. Groene, A. M. Persoon, J. D. Menietti, S.-Y. Ye, W. S. Kurth, R. J. MacDowell, and A. Lecacheux (2010b), The reversal of the rotational modulation rates of the north and south components of Saturn kilometric radiation near equinox, *Geophys. Res. Lett.*, *37*, L24101, doi:10.1029/2010GL045796.
Hunt, G. J., S. W. H. Cowley, G. Provan, E. J. Bunce, I. I. Alexeev, E. S. Belenkaya, V. V. Kalegaev, M. K. Dougherty, and A. J. Coates (2014), Field-aligned currents in Saturn's southern nightside magnetosphere: Subcorotation and planetary period oscillation components, *J. Geophys. Res. Space Physics*, *119*, 9847–9899, doi:10.1002/2014JA020506.
Hunt, G. J., S. W. H. Cowley, G. Provan, E. J. Bunce, I. I. Alexeev, E. S. Belenkaya, V. V. Kalegaev, M. K. Dougherty, and A. J. Coates (2015), Field-aligned currents in Saturn's southern nightside magnetosphere: Field-aligned currents in Saturn's northern nightside magnetosphere—Evidence for interhemispheric current flow associated with planetary period oscillations, *J. Geophys. Res. Space Physic*, *120*, doi:10.1002/2015JA021454.
Kaiser, M. L., M. D. Desch, J. W. Warwick, and B. Pearce (1980), Voyager detection of nonthermal emission from Saturn, *Science*, *209*, 1238–1240.
Kanani, S. J., et al. (2010), A new form of Saturn's magnetopause using a dynamic pressure balance model, based on in situ, multi-instrument Cassini measurements, *J. Geophys. Res.*, *115*, A06207, doi:10.1029/2009JA014262.
Kimura, T., et al. (2013), Long-term modulations of Saturn's auroral radio emissions by the solar wind and seasonal variations controlled by solar ultraviolet flux, *J. Geophys. Res. Space Physics*, *118*, 7019–7035, doi:10.1002/2013JA018833.
Krupp, N., et al. (2005), The Saturnian plasma sheet as revealed by energetic particle measurements, *Geophys. Res. Lett.*, *32*, L20S03, doi:10.1029/2005GL022829.
Kurth, W. S., A. Lecacheux, T. F. Averkamp, J. B. Groene, and D. A. Gurnett (2007), A Saturn longitude system based on a variable kilometric radiation period, *Geophys. Res. Lett.*, *34*, L02201, doi:10.1029/2006GL028336.
Kurth, W. S., T. F. Averkamp, D. A. Gurnett, J. B. Groene, and A. Lecacheux (2008), An update to a Saturnian longitude system based on kilometric radio emissions, *J. Geophys. Res.*, *113*, A05222, doi:10.1029/2007JA012861.
Lamy, L., R. Prangé, W. Pryor, J. Gustin, S. V. Badman, H. Melin, T. Stallard, D. G. Mitchell, and P. C. Brandt (2013), Multispectral diagnosis of Saturn's aurorae throughout a planetary rotation, *J. Geophys. Res. Space Physics*, *118*, 4817–4843, doi:10.1002/jgra.50404.
Masters, A., N. Achilleos, M. K. Dougherty, J. A. Slavin, G. B. Hospodarsky, C. S. Arridge, and A. J. Coates (2008), An empirical model of Saturn's bow shock: Cassini observations of shock location and shape, *J. Geophys. Res.*, *113*, A10210, doi:10.1029/2008JA013276.
Meredith, C. J., S. W. H. Cowley, and J. D. Nichols (2014), Survey of Saturn auroral storms observed by the Hubble Space Telescope: Implications for storm time scales, *J. Geophys. Res. Space Physics*, *119*, 9624–9642, doi:10.1002/2014JA020601.
Nichols, J. D., J. T. Clarke, S. W. H. Cowley, J. Duval, A. J. Farmer, J.-C. Gérard, D. Grodent, and S. Wannawichian (2008), Oscillation of Saturn's southern auroral oval, *J. Geophys. Res.*, *113*, A11205, doi:10.1029/2008JA013444.
Nichols, J. D., B. Cecconi, J. T. Clarke, S. W. H. Cowley, J.-C. Gérard, A. Grocott, D. Grodent, L. Lamy, and P. Zarka (2010a), Variation of Saturn's UV aurora with SKR phase, *Geophys. Res. Lett.*, *37*, L15102, doi:10.1029/2010GL044057.
Nichols, J. D., S. W. H. Cowley, and L. Lamy (2010b), Dawn-dusk oscillation of Saturn's conjugate auroral ovals, *Geophys. Res. Lett.*, *37*, L24102, doi:10.1029/2010GL045818.
Prangé, R., L. Pallier, K. C. Hansen, R. Howard, A. Vourlidas, R. Courtis, and C. Parkinson (2004), An interplanetary shock traced by planetary auroral storms, *Nature*, *432*, 78–81.
Prise, A. J., L. K. Harra, S. A. Matthews, C. S. Arridge, and N. Achilleos (2015), Analysis of a coronal mass ejection and corotating interaction region as they travel from the Sun passing Venus, Earth, Mars, and Saturn, *J. Geophys. Res. Space Physics*, *120*, 1566–1588, doi:10.1002/2014JA020256.
Provan, G., D. J. Andrews, C. S. Arridge, S. W. H. Cowley, S. E. Milan, M. K. Dougherty, and D. M. Wright (2009a), Polarization and phase of planetary period oscillations on high latitude field lines in Saturn's magnetosphere, *J. Geophys. Res.*, *114*, A02225, doi:10.1029/2008JA013782.
Provan, G., S. W. H. Cowley, and J. D. Nichols (2009b), Phase relation of oscillations near the planetary period of Saturn's auroral oval and the equatorial magnetospheric magnetic field, *J. Geophys. Res.*, *114*, A04205, doi:10.1029/2008JA013988.
Provan, G., D. J. Andrews, B. Cecconi, S. W. H. Cowley, M. K. Dougherty, L. Lamy, and P. M. Zarka (2011), Magnetospheric period magnetic field oscillations at Saturn: Equatorial phase "jitter" produced by superposition of southern and northern period oscillations, *J. Geophys. Res.*, *116*, A04225, doi:10.1029/2010JA016213.
Provan, G., D. J. Andrews, S. W. H. Cowley, J. Sandhu, and M. K. Dougherty (2013), Planetary period oscillations in Saturn's magnetosphere: Abrupt and non-monotonic transition to northern oscillation dominance two years after equinox, *J. Geophys. Res. Space Physics*, *118*, 3243–3264, doi:10.1002/jgra.50186.

Provan, G., L. Lamy, S. W. H. Cowley, and M. K. Dougherty (2014), Planetary period oscillations in Saturn's magnetosphere: Comparison of magnetic oscillations and SKR modulations in the postequinox interval, *J. Geophys. Res. Space Physics*, *119*, 7380–7401, doi:10.1002/2014JA020011.

Sandel, B. R., and A. L. Broadfoot (1981), Morphology of Saturn's aurora, *Nature*, *292*, 679–682.

Sandel, B. R., et al. (1982), Extreme ultraviolet observations from the Voyager 2 encounter with Saturn, *Science*, *215*, 548–553.

Seaton, D. B., et al. (2013), The SWAP EUV imaging telescope. Part I: Instrument overview and pre-flight testing, *Sol. Phys.*, *286*(1), 43–65.

Southwood, D. J., and M. G. Kivelson (2007), Saturn magnetospheric dynamics: Elucidation of a camshaft model, *J. Geophys. Res.*, *112*, A12222, doi:10.1029/2007JA012254.

Tao, C., R. Kataoka, H. Fukunishi, Y. Takahashi, and T. Yokoyama (2005), Magnetic field variations in the Jovian magnetotail induced by solar wind dynamic pressure enhancements, *J. Geophys. Res.*, *110*, A11208, doi:10.1029/2004JA010959.

Warwick, J. W., et al. (1981), Planetary radio astronomy observations from Voyager-1 near Saturn, *Science*, *212*, 239–243.

Warwick, J. W., D. S. Evans, J. H. Romig, J. K. Alexander, M. D. Desch, M. L. Kaiser, M. Aubier, Y. Leblanc, A. Lecacheux, and B. M. Pedersen (1982), Planetary radio astronomy observations from Voyager-2 near Saturn, *Science*, *215*, 582–587.

Young, D. T., et al. (2004), Cassini Plasma Spectrometer investigation, *Space Sci. Rev.*, *114*, 1–112, doi:10.1007/s11214-004-1406-4.

Zarka, P., L. Lamy, B. Cecconi, R. Prangé, and H. O. Rucker (2007), Modulation of Saturn's radio clock by solar wind speed, *Nature*, *450*, 265–267, doi:10.1038/nature06237.

Zieger, B., and K. C. Hansen (2008), Statistical validation of a solar wind propagation model from 1 to 10 AU, *J. Geophys. Res.*, *113*, A08107, doi:10.1029/2008JA013046.